Inorganic and Metal-Organic Framework Materials

-Synthesis and structure characterization

Leifeng Liu


UNIVERSITET STOCKHOLMS
Stockholm
University

Inorganic and Metal-Organic Framework Materials

-Synthesis and structure characterization

Leifeng Liu

ISBN 978-91-7447-913-3

Printed in Sweden by Printers name, City 20XX
Distributor: Name of distributor (usually the department)

To My grandfather, Piluo Liu.

The sense of achievement only comes from the accomplishment of your real goal.

-Dr. Zhengrong Shi

Abstract

Inorganic and metal-organic framework materials possessing accessible and permanent pores are receiving tremendous attention. Among them, zeolites are the most famous class due to their wide applications on petrochemistry and gas separation. Besides zeolites, the other oxide framework materials are also intensively investigated because of their diverse structures and compositions. Metal-organic frameworks are built from metal clusters and organic linkers. By rational designing the reagent, the network with desired topology and functionality can be synthesized.

For all of the framework materials mentioned above, to explore novel framework structures is important for improving properties and discovering new applications. This thesis includes the synthesis of zeolites and structure characterization for various types of inorganic framework materials. The zeolite synthesis conditions were exploited. With the optimized condition, the zeolite ITQ-33 was synthesized as single crystals. From the single crystal X-ray diffraction data, the disorder in the structure is discovered and explained. Following the topic of disorder and twinning, we proposed a novel method of solving structure of pseudo-merohedric twinning crystal by using an example of a metal-organic complex crystal. Then we also showed methods for solving structures of high complexity and nano-crystal by using mainly powder X-ray diffraction and transmission electron microscopy. Four examples were shown in chapter 4 including open-framework germanates and metal-organic frameworks.

Keywords: X-ray diffraction, transmission electron microscopy, framework materials, porous materials.

List of papers

This thesis is based on paper I to paper VI:

I. Disorder in Extra-large Pore Zeolite ITQ-33 Revealed by Single Crystal XRD.
Liu, L.; Yu, Z.; Chen, H.; Li, B. and Sun, J.
Cryst. Growth Des., **2013**, 13, 4168-4171
My contribution: synthesis, structure determination and major contributions towards the manuscript writing.

II. Structure Determination of [3Fe2S] Complex with Complicated Pseudo-Merohedric Twinning.
Liu, L.; Li, M.; Gao, W.; Åkermark, B. and Sun, J.
Z. Kristallogr., **2012**, 227, 221-226
My contribution: structure determination and the major contributions towards the manuscript writing.

III. Germanate with Three-Dimensional 12×12×11-Ring Channels Solved by X-ray Powder Diffraction with Charge-Flipping Algorithm.
Xu, Y.#; Liu, L.#; Chevrier D.M.; Sun, J.; Zhang, P. and Yu, J.
Inorg. Chem., 2013, 52, 10238-10244
#Authors with equal contribution.
My contribution: structure determination and contributions towards the manuscript writing on structure determination and description parts.
.

IV. Metal-Oxide Nanoparticles with Desired Morphology Inherited from Coordination-Polymer Precursors.
Zhao, J.; Li, M.; Sun, J.; Liu, L.; Su, P.; Yang, Q. and Li, C.
Chem. Eur. J., 2012, 18, 3163-3168

My contribution: structure determination and contributions towards the manuscript writing on structure determination and description parts.

V. SU-77: an open-framework germanate containing 12 × 10 × 10-ring channels solved by combining rotation electron diffraction and powder X-ray diffraction.
Fang, L. #; Liu, L.#; Yun, Y.; Inge, A.K.; Wan, W.; Zou, X. and Gao, F.
Cryst. Growth Des., to be submitted.
#Authors with equal contribution
My contribution: structure determination and major contributions towards the manuscript writing

VI. Irreversible Network Transformation in a Dynamic Porous Host Catalyzed by Sulfur Dioxide.
Yang, S; Liu, L.; Sun J.; Thomas, K.M.; Davies, A.J.; George, M.W.; Blake, A.J.; Hill, A.H.; Fitch, A.N.; Tang, C. and Schröder, M.
J. Am. Chem. Soc., 2013, 135, 4954-4957
My contribution: structure determination and contributions towards the manuscript writing on structure determination and description parts.

Papers not included in the thesis:

VII. Synthesis, Characterization and Catalytic properties of Titansilicate and Vanadosilicate Hierarchical-porous materials from Nano-building Blocks.
Liu, L.; Yu, Z.; Zheng H.; Sun, J.,
in manuscript
My contribution: synthesis, structure determination and major contributions towards the manuscript writing.

VIII. Ab initio Structure Determination of Interlayer Expanded Zeolites by Single Crystal Rotation Electron Diffraction.
Guo, P.; Liu, L.; Yun, Y.; Su J.; Wan, W.; Gies, H.; Zhang, H.; Xiao, F.; Zou, X.,
Dalton Trans., DOI:10.1039/C4DT00458B.
My contribution: involves in structure determination and contributions towards the manuscript writing.

IX. Structure analysis of zeolites by rotation electron diffraction (RED).
Su, J.; Kapaca, E.; Liu, L.; Georgieva, V.; Wan, W.; Sun, J.; Valtchev, V.; Hovmöller, S.; Zou, X.;
Microporous Mesoporous Mater., **2013**,
http://dx.doi.org/10.1016/j.micromeso.2013.10.014
My contribution: synthesis and minor contributions towards the manuscript writing.

X. Achiral Co-Catalyst Induced Switches in Catalytic Asymmetric Reactions on Racemic Mixtures (RRM): From Stereodivergent RRM to Stereoconvergent Deracemization by Combination of Hydrogen Bond Donating and Chiral Amine Catalysts.
Ma, G.; Lin, S.; Ibrahem, I.; Kubik, G.; Liu, L.; Sun, J. and Cordova, A.;
Adv. Synth. Catal., **2012**, 354, 2865-2872
My contribution: structure determination.

XI. A Palladium/Chiral Amine Co-catalyzed Enantioselective Dynamic Cascade Reaction: Synthesis of Polysubstituted Carbocycles with a Quaternary Carbon Stereocenter.
Ma, G.; Afewerki, S.; Deiana, L.; Palo-Nieto, C.; Liu, L.; Sun, J.; Ibrahem, I. and Córdova, A.
Angew. Chem. Int. Ed., **2013**, 52, 6050-6054
My contribution: structure determination.

Contents

1 Introduction 15
1.1 Inorganic framework materials 16
1.1.1 Zeolites 16
1.1.2 Open germanate frameworks 22
1.1.3 Metal-organic frameworks 24
1.2 Crystal and diffraction 26
1.2.1 Basics of crystallography 26
1.2.2 X-ray diffraction 30
1.2.3 Electron diffraction 35
1.3 Objectives and contents of this thesis 36

2 Synthesis and structure characterization using diffraction methods 37
2.1 Synthesis of zeolites 37
2.2 Diffraction methods 39
2.3 Single crystal X-ray diffraction 39
2.4 Powder X-ray diffraction 43
2.5 Transmission electron microscopy 47

3 Disordered and twinned structures determined by using single crystal XRD 49
3.1 Disorder in extra-large pore zeolite ITQ-33 (paper I) 49
3.2 Method for solving structure of a Pseudo-merohedric twinned crystal (paper II) 55

4 Structure characterization from powder XRD 60
4.1 Complicated structure of GeO-JU90 germanate determined by PXRD (paper III) 60
4.2 Structure of Zn-ptcda MOF determined by PXRD (paper IV) 64
4.3 Germanate SU-77 determined by combining TEM and PXRD (paper V) 66
4.4 Characterization of structure transformation of NOTT-202 MOF by in-situ PXRD (paper VI) 70

5 Conclusions and future work 75

6 Acknowledgements 77

7 Reference 79

8 Appendix 86

Abbreviations

ADT	Automated diffraction tomography
BTC	1,3,5-benzenetricarboxylate
CBU	Composite building unit
D3R	Double 3-ring
D4R	Double 4-ring
EXAFS	Extended X-ray absorption fine structure
FCC	Fluid catalytic cracking
HRTEM	High-resolution transmission electron microscopy
IZA	International Zeolite Association
L^{4-}	Bipyenyl-3, 3', 5, 5'-tetra-(phenyl-4-carboxylate)
MOF	Metal-organic framework
MTO	Methanol-to-Olefins
NaKA	Sodium/potassium form of zeolite A
NMR	Nuclear magnetic resonance
ptcda	Perylene-3, 4, 9, 10-tetracarboxylic dianhydride
PXRD	Powder x-ray diffraction
RED	Rotation electron diffraction
SAED	Selected area electron diffraction
SBU	Secondary building unit
SEM	Scanning electron microscopy
SDA	Structure directing agent
SXRD	Single crystal X-ray diffraction
T-atoms	Tetrahedrally coordinated framework atoms
TEM	Transmission electron microscopy
TESO	Tetraethyl orthosilicate

TGA	Thermogravimetric analysis
XRD	X-ray diffraction

1 Introduction

Inorganic framework and metal-organic framework (MOF) materials possessing accessible and permanent pores are receiving tremendous attraction from chemists, physicists and materials scientists from all over the world because of their commercial interests on various applications.[1] Among inorganic framework materials, the most important class is zeolites which are frameworks of tetrahedrally coordinated crystalline oxides. Besides zeolites, many classes of materials of oxides not limited to 4-coordination are also intensively investigated, for instance, titanosilicates, germanium oxides and transition metal phosphates.[2–4]

MOFs are a kind of framework materials built of metal clusters and organic linkers. By rational design of the reagents, network with desired topology and functionality can be synthesized.[5]

According to the pore sizes, porous materials can be categorized into three classes: microporous materials with pore sizes below 2 nm, mesoporous materials with pore sizes between 2 nm and 50 nm and macroporous materials with pore sizes larger than 50 nm.[6,7] The majority of inorganic framework materials fall into the category of microporous materials. However, recently, more and more inorganic frameworks with mesopores have been synthesized. Germanosilicate zeolite ITQ-43 is the first zeolite with pore window larger than 20 Å (21.9 Å).[8] A series of gallium zincophosphites with one dimensional channels of various sizes ranging from 6.9 Å to 35 Å were synthesized by rational design of the template molecules.[9] Moreover, even larger pore sizes has been archived for MOFs. IRMOF-74 is a remarkable example which possesses a 98 Å pore opening with 282 atoms in a ring.[10]

The most well-known applications of porous framework materials are in ion-exchange, gas and liquid separation, oil cracking and petrochemical production.[11,12] For all of these applications, crystal structures are critical to the performances. The crystal structures not only determine the sizes of the apertures but also the dimensions of the

channels, the shape and connectivity of the channels and the arrangements of the cages.[13] Therefore the studies on synthesis and structure characterization are of great importance to the development of this research field.

1.1 Inorganic framework materials

1.1.1 Zeolites

In 1756, an interesting phenomenon was observed by the Swedish mineralogist Axel F. Cronstedt when he was heating a newly discovered silicate mineral.[14] He found the mineral underwent intumescence and fused readily when heated in a flame of blowpipe. He then named this mineral "zeolite" which was derived from Greek words, "zeo" and "lithos" meaning "to boil" and "a stone".[15] Zeolites hadn't drawn too much attention until they were synthesized through hydrothermal reaction in early 1940s by Richard Barrer.[16] A few years later, Robert Milton from the laboratories of Linde Corporation synthesized zeolite chabazite.[17] It was a significant step forward because the scarce natural counterpart was the only choice of material found to be suitable for industrial air separation and purification applications.[17] Two decades later, in 1960s, another important progress in zeolite synthesis was made by Barrer and Denny by introducing quaternary organic ammonium in the synthesis.[18] In 1967, the first high-silica zeolite (zeolite β) was disclosed initiating the era of zeolites in the field of materials and catalysis.[16]

Strictly speaking, zeolites must be hydrated crystalline frameworks of tectoaluminosilicates built from TO_4 tetrahedra where T denotes tetrahedral Si and Al and each oxygen atom is corner-shared by two adjacent tetrahedra as shown in Figure 1.1.[14] The anionic frameworks are compensated by cations located at the pores and loosely bound to the oxygen atoms in the framework.[19] However, with the development of synthetic routes of zeolites, the definition of zeolite has been significantly broadened. First of all, T atoms in the frameworks are no longer limited to Si and Al. For example, boron, phosphorus and germanium can be included as well. The introduction of such atoms not only enriches the chemistry of zeolites but also brings in diverse framework topologies due to the differences in lengths, angles and the flexibility of the bonds[20]. Secondly, the definition of guest species has

been expanded to include both inorganic cations and organic molecules, e.g. quaternary ammonium. The utilization of organic molecules in zeolite synthesis as structure directing agents (SDA) greatly accelerated the discovery of large and extra-large pore zeolites as well as zeolites with high ratio of quadrivalent atoms to trivalent atoms[16,21].

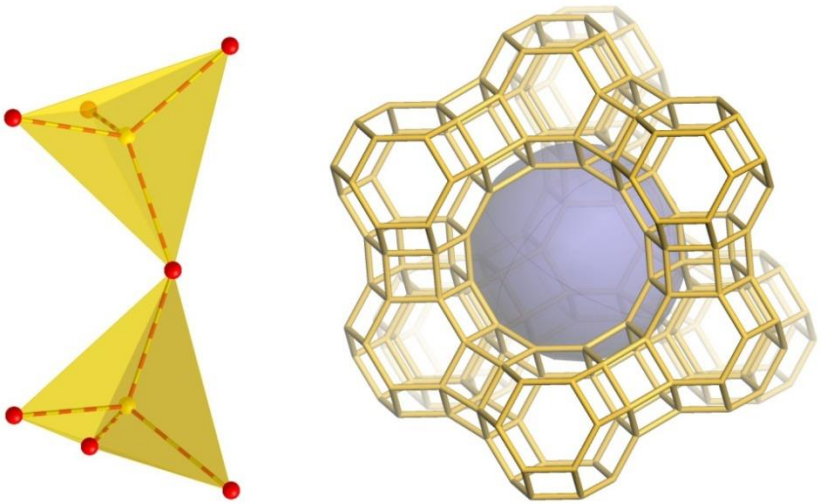

Figure 1.1 (a) Two SiO_4 tetrahedra connected by a bridging oxygen atom (yellow: Si, red: oxygen); (b) the idealized framework of FAU zeolite (oxygen atoms are omitted, the purple sphere represents the cavity surrounded by nine SOD cages).

Crystallization mechanism

Since the successful synthesis of zeolites through the hydrothermal method, researchers are particularly interested in understanding the crystallization mechanisms of zeolites. However, due to the complexity of the reaction which involves both solid and liquid, a comprehensive theory of zeolite crystallization is still lacking. There are mechanisms proposed by different research groups. In a paper by Breck, a scheme of zeolite crystallization was given for the first time.[22] He showed that the gel structure was firstly depolymerized and then polyhedra formed through the rearrangement of aluminoslicate and silicate anions in the gel. The polyhedra connect to form crystals. This mechanism is referred to solid-phase transformation as the process involves only the rearrangement of an amorphous phase. Besides the solid-phase transformation, there are also proposed mechanisms involving the liquid phase. Kerr and Ciric proposed the solution-mediated

transformation theory of zeolite crystallization[23] which suggests that the gel first dissolves in the solution and then precipitates out from the solution to form zeolite crystals.

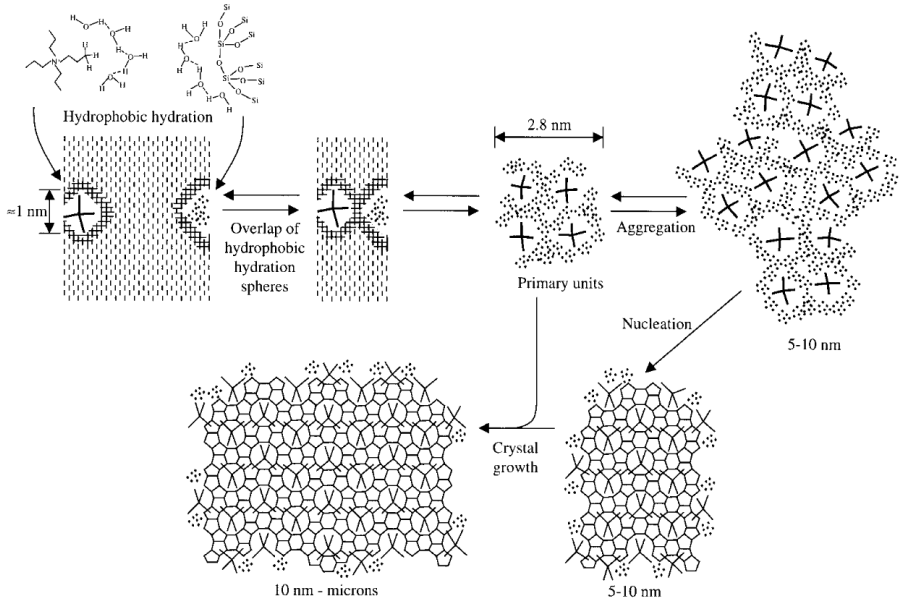

Figure 1.2 Scheme for the crystallization process of zeolite MFI by de Moor.[24]

Recent progress in the understanding of zeolite formation inclines to the mechanism involving both liquid-phase and solid-phase. As described in de Moor's paper[24], after investigating the process by using techniques including small-angle and wide angle X-ray scattering, he draw the scheme for the MFI zeolite crystallization mechanism as shown in Figure 1.2. At the beginning of the process, hydrophobic spheres are formed surrounding both the SDAs (tetrapropyl ammonium cation) and silicates. Then the overlap of such spheres drives the formation of nanometer sized primary building units comprising SDAs and silicate. During the nucleation, primary units aggregate and turn to ordered structures, up to the size of 10 nm. Although it has been more than 70 years since Richard Barrer synthesized the first zeolite in laboratory, the mechanism of zeolite formation is still not fully understanding

Building units

At present, there are 218 zeolite framework types approved by the International Zeolite Association. Some common structural features such as cavities and chains can be found in different frameworks. These

structure features not only help researchers to understand the structures more easily, but also provide hints to synthesis and properties. Figure 1.3 shows some building units frequently presented in zeolite frameworks.

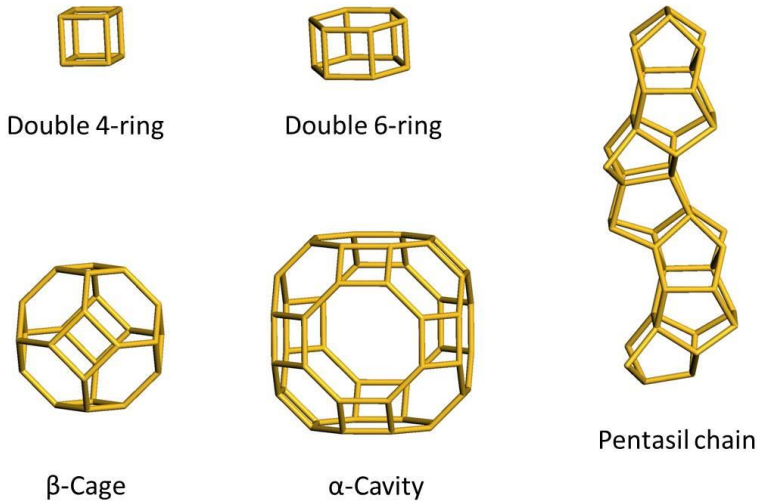

Figure 1.3 Some building units that recur in zeolite frameworks (oxygen atoms are omitted).

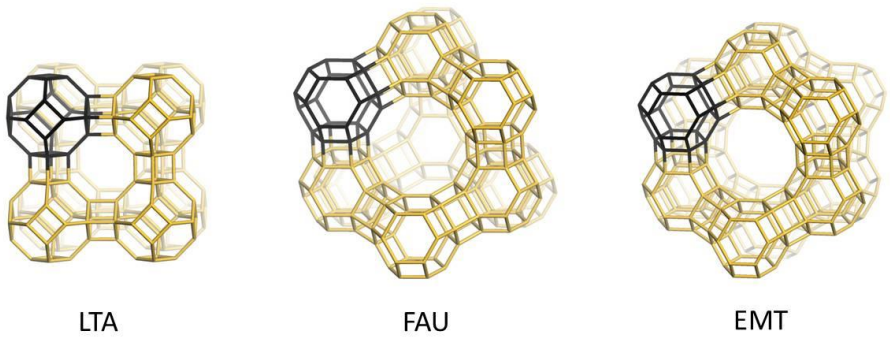

Figure 1.4 Zeolites built up from SOD cage (oxygen atoms are omitted).

Several widely used zeolites are built up based on a common unit, the β-cage (also called SOD cage), but with different connecting schemes. In the LTA zeolite, the framework can be described as the β-cages arranged in a primitive cubic way, connecting the neighbors through double 4-rings. In FAU and EMT zeolites, the β-cages connect through double 6-rings, but the way β-cages arranged is different. For the FAU zeolite, β-cages are arranged in the same way as carbon atoms

in the diamond structure. This is also one of the reasons for the excellent thermal stability of the FAU zeolite. For the EMT zeolite, β-cages build up the same layer as that in FAU, but the layers are stacked in an ABAB sequence in EMT instead of the ABC sequence in FAU.

Relations between zeolites structures and applications

Crystal structure is the most crucial factor for the application of zeolites. The reason is that the crystal structures define the channels in the zeolites, which determine the accessibility of the pore, transportation rate of the guest molecules and many other important factors. Small difference in the crystal structures can result in big differences in their performances.

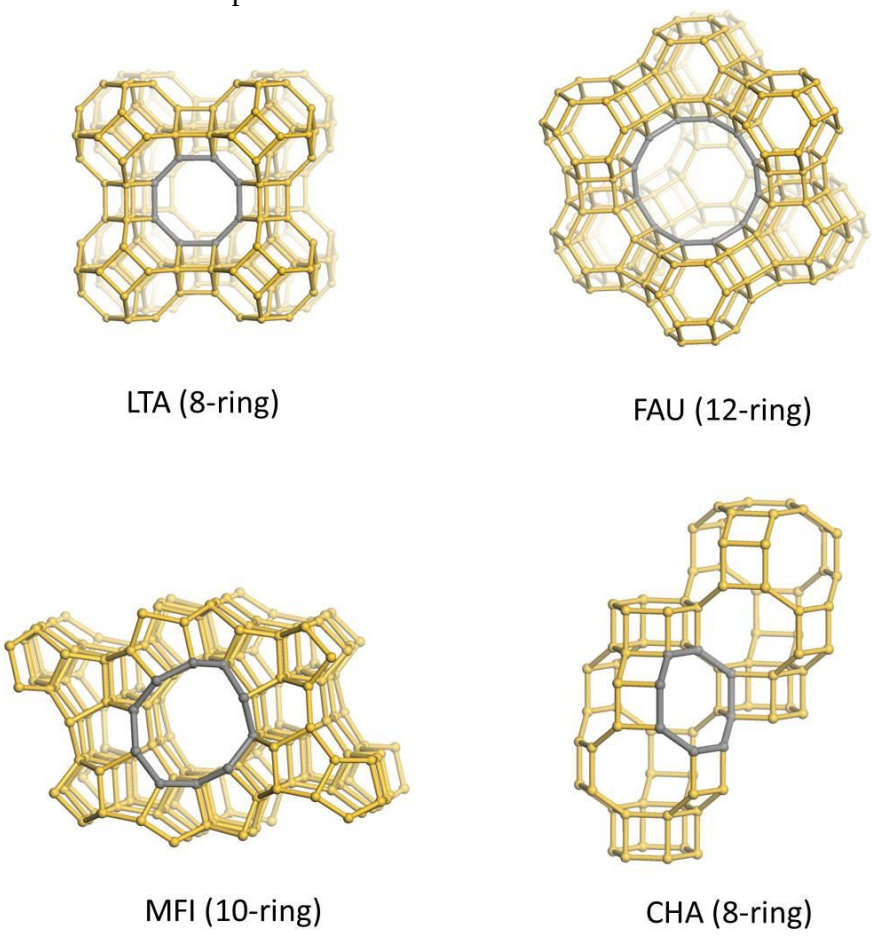

Figure 1.5 Frameworks of LTA, FAU, MFI and CHA type zeolites. Oxygen atoms are omitted to simplify the structure models. Pore openings are marked in grey.

Zeolite A is the abbreviation of the Linde Type A zeolite typically

with the composition of $Na_{12}Al_{12}Si_{12}O_{48}$. The sodium cations in the channel can be replaced by calcium cations to produce the calcium form of zeolite A, CaA. As shown in Figure 1.5, zeolite A is a small pore zeolite with an aperture of 8-ring. One of the most important applications of zeolite A is to replace phosphate as the builder in laundry detergent for removing the hard Ca^{2+} and Mg^{2+} cations[25]. Sodium form of zeolite A shows high selectivity and capability to exchange Ca^{2+} and Mg^{2+} cations in water by Na^{+} cations. Besides the application in ion exchange, the sodium/potassium form of zeolite A (NaKA) is one of the most promising solid adsorbents for carbon dioxide[26]. Utilizing the small difference between kinetic diameters of CO_2 and N_2 (0.33 nm for CO_2 and 0.36 nm for N_2), the NaKA with tunable pore sizes in the range between 0.3 nm and 0.38 nm shows excellent CO_2-over-N_2 selectivity in gas absorption.[27]

Zeolite Y with the framework type of FAU is the main catalyst for petrochemical industry, for example fluid catalytic cracking (FCC), hydrocracking and alkylation.[28] The cavity with diameter of around 13 Å in zeolite Y is surrounded by 10 β-cages and has 4 large pore openings (12-ring). This unique structure feature of zeolite Y ensures the fast diffusion of reagents and products in zeolite crystals. In addition, zeolite Y also shows strong acidity and ultra-high stability under harsh conditions, which makes it the leading catalyst in the petrochemical industry.[29]

Zeolite ZSM-5 is another important catalyst in oil refining and many other petrochemistry processes. ZSM-5 is a medium-pore zeolite built up by pentasil chains. In the structure of ZSM-5 there are three-dimensional inter-connected 10-ring channels, among which one is straight and the other two are running in a zigzag way in the plane perpendicular to the straight channel. Comparing to the large pore size of around 7.4 Å for zeolite Y, the pore aperture of ZSM-5 is only around 5.3 Å.[19] The difference in pore size and the way the channels run induce significant differences in the catalytic performances. For instance, in the FCC process, ZSM-5 is used as an additive to the main catalyst of zeolite Y. Due to the small pore size of ZSM-5, molecules larger than monomethyl aliphatics and the molecules with critical diameters larger than 6 Å are severely limited to diffuse into the channels with active sites. The straight chain C_7+ aliphatics that are small enough to enter the pores are mainly cracked into C_3 to C_5 olefins. Hence the addition of ZSM-5 results in a considerable increase of the yield of small alkenes (propene and butenes) which are products more desired than gasoline,

due to their higher market price.[30,31] At the same time, the linear and mono-branched C_7+ aliphatics convert to small alkenes causing an increased fraction of aromatics and isopentene in gasoline product and thereby increasing the octane number of the gasoline.[30,31]

SAPO-34 zeolite is an aluminium phosphate with some phosphorus sites replaced by silicon. The underlying topology (CHA) of SAPO-34 is the same as the natural occurring mineral chabazite. As shown in Figure 1.5, the structure is built up by connecting the double 6-rings through 4-rings. It has relative large cavities but small 8-ring openings. This structural feature and the moderate acid strength give SAPO-34 outstanding selectivity on the Methanol-to-Olefins (MTO) process.[32] As explained by a widely accepted mechanism (hydrocarbon pool mechanism) of the MTO reaction, the large chabazite cages can trap the active reaction intermediates, polyalkyl aromatics, inside. Catalyzed by Brønsted acid sites of the framework, the reactive intermediates turn into light olefins.[33] In addition, the small 8-ring aperture with diameter of around 3.8 Å inhibits the diffuse of heavy and branched hydrocarbons leading to the high selectivity to the desired light olefins.[33,34]

1.1.2 Open germanate frameworks

As discussed above, crystal structure is a key factor for applications of framework materials. To enrich the choices of materials for potential applications[35], framework materials with novel topologies are desirable.

Germanium, the element just below silicon in the periodic table of elements, has been studied intensively as a framework element to extend the structure diversity of microporous materials[36]. Although germanium is in the same group as silicon, their coordination behaviors are quite different[37]. Silicon forms tetrahedra with oxygen atoms in all cases except at some extreme conditions e.g. ultra high pressure[38]. Due to the larger radius of the germanium atom, its coordination with oxygen is much more flexible. It can be 4-, 5-, or 6-coordinated to oxygen atoms. This flexibility gives rise to the diverse framework topologies of the germanates.

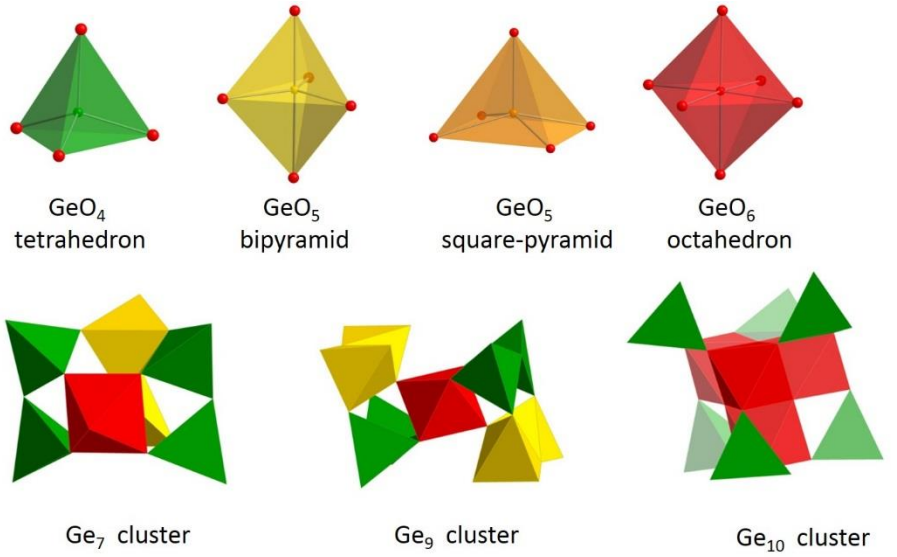

Figure 1.6 Germanium oxide polyhedra and composite building units. Oxygen atoms are in red. GeO_4 tetrahedra are in green, GeO_5 bipyramids or square-pyramids are in yellow and GeO_6 octahedra are in red.

In the germanate frameworks there are four commonly occurring primary building units. They are shown in Figure 1.6 (GeO_4 tetrahedron, GeO_5 trigonal bipyramid, GeO_5 square pyramid and GeO_6 octahedron). Composed of these polyhedra, a number of clusters (shown in Figure 1.6) are frequently found as composite building units in germanate frameworks[39–41]. Since these clusters are relatively large in size, when linking these clusters together to form frameworks, it is not rare to obtain frameworks with extra-large pores. Figure 1.7 shows the framework of SU-M[42]. It was the largest primitive cell and lowest framework density of all inorganic materials at that time. With the 30-ring channels in the structure, SU-M has the largest pore aperture found: 25.1 Å, which already lies in the mesopore range.

In addition, replacing silicon by germanate enriches the framework types by offering different bond lengths and bond angles even at tetrahedral coordination condition. The longer bond length (Ge-O: 1.74 Å; Si-O: 1.61 Å) and significantly smaller bond angle (Ge-O-Ge $\geq 130^o$; Si-O-Si $\geq 145^o$) for tetrahedrally coordinated germanium than silicon induce significant changes in the framework formation[43]. Commonly, germanium facilitates the formation of small rings as the building units in the structures, e.g. double 4-rings, double 3-rings and 3-rings[35]. A number of extraordinary zeolitic frameworks were synthesized using germanium as T-atoms. GaGeO-CJ63 is a gallogermanate zeolite with

Ga/Ge=1/2 [44]. The framework is constructed exclusively of 3-ring building units and with very low framework density of 10.5T/1000Å^3 [44].

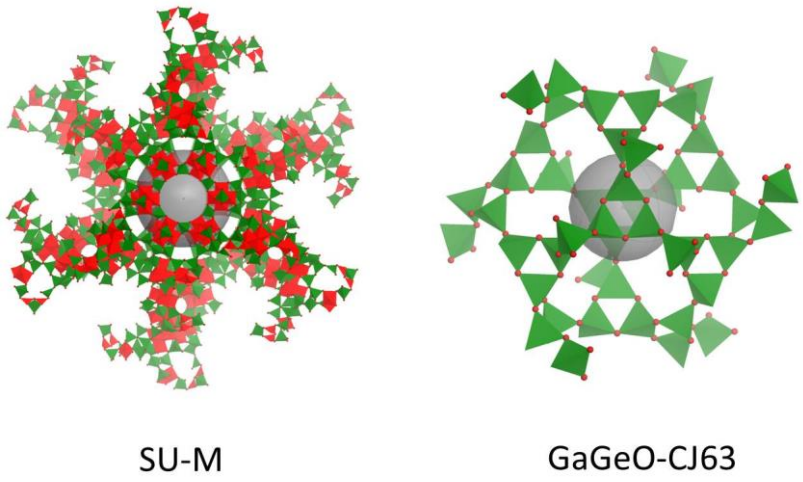

Figure 1.7 Structures of SU-M and GaGeO-CJ63 represented in polyhedra form.GeO_4 tetrahedra are in green, GeO_6 octahedra are in red and the red balls denote the oxygen atoms[42,44].

1.1.3 Metal-organic frameworks

Recently, much attention in the field of porous materials has been focused on the design and synthesis of MOFs[45]. This class of materials renewed the concept of hydrothermal synthesis toward the direction of rational design[5]. Besides, the exceptional properties of this class of materials e.g. high surface area and porosity, organic functionality and tunable metrics imply great application potential[5,12].

Building units

It is believed that the lack of control on products in traditional synthetic methods is due to the starting reagents not maintaining their structures during the reaction.[5] In contrast, MOFs are built up by the assembly of rigid molecular building blocks which include inorganic secondary building units (SBU) and organic linkers[46]. Under appropriate synthesis conditions, it is possible to obtain desired inorganic SBUs and retain the structural integrity of the organic linkers. Through strong coordination bonding, these two components connect to form frameworks[47]. This SBU approach leads the final structure of

the MOF crystal towards a small number of preferred topologies. These can be predicted or targeted before the synthesis[48]. Figure 1.8 shows some inorganic secondary building units and organic linkers which are frequently used in MOF synthesis.

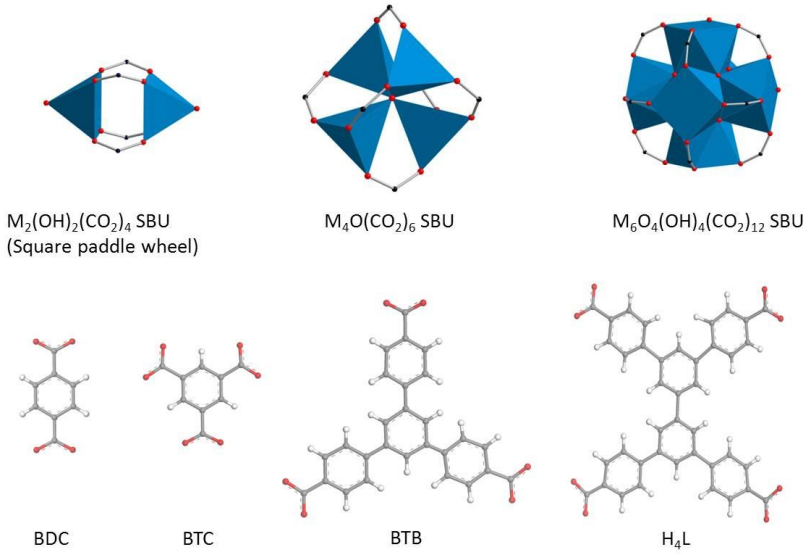

Figure 1.8 Secondary building units and organic linkers. M:metal; BDC: 1,4-benzene dicarboxylate; BTC: 1,3,5-benzene tricarboxylate; BTB: benzene-1,3,5-tribenzoate; H4L: biphenyl-3, 3',5, 5'-tetra-(phenyl-4-carboxylic acid).

Relation between properties and structures

HKUST-1 composed of copper ions coordinated by 1,3,5-benzenetricarboxylate (BTC) linkers is named after the Hong Kong University of Science and Technology. HKUST-1 was first synthesized in 1999. It is among the most investigated MOFs due to its excellent adsorption properties, high stability and also its simplicity[49]. The pore size of HKUST-1 is far from large among MOF materials. It has three kinds of pores among which the smallest one is around 4 Å in diameter and the two larger ones are around 10 Å in diameter. Due to the small accessible pores and the open metal sites in the structure, HKUST-1 is the bench mark material for methane storage[50,51]. According to the report published by researchers from NIST, as one of the earliest MOFs, HKUST-1 still owns the exceptionally high volumetric methane uptake properties of 267 cc(STP)/cc at 65 bar which is slightly higher than the target set by US Department of Energy[52].

UiO-66 is a zirconium MOF made by researchers from University of Oslo[53]. It receives lots of attention because of its exceptional stability.

It stays intact up to 500 °C in air, is stable in water and most organic solvents, and also shows excellent stability under mechanical stress[54]. It is believed that the stability is mainly attributed to the unique inorganic building units in the UiO-66 structure. Zirconium has the valence of +4 and binds strongly to oxygen atoms. Each inorganic building unit of UiO-66 is composed of six zirconium oxygen polyhedra and twelve carboxylate groups[55,56]. Such a high coordination number of the clusters also benefits the stability of the material[53].

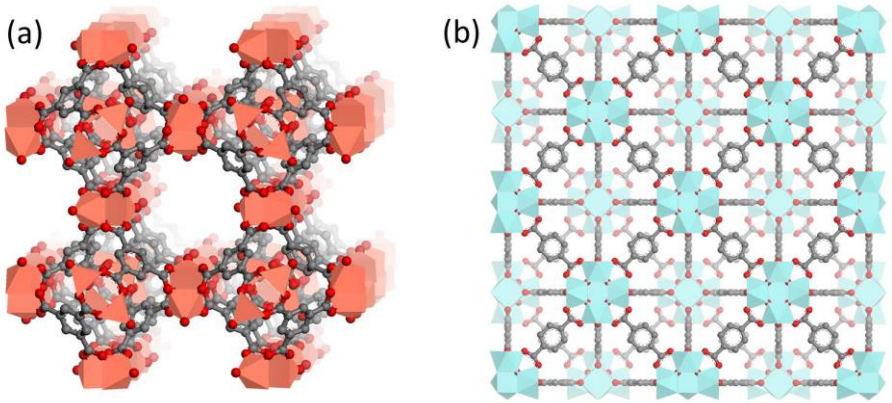

Figure 1.9 Structures of (a) HKUST-1 and (b) UiO-66. Black: carbon atoms; red: oxygen atoms; orange: copper-oxygen polydedra; blue: zirconium-oxygen polyhedra[53,57].

1.2 Crystal and diffraction

As discussed above, the crystal structures determine some crucial parameters of the inorganic framework materials for their applications. To determine crystal structures, diffraction methods are the most powerful ones. Diffraction methods have been intensively used to determine and identify crystal structures since they were discovered in November, 1912. Back then, William Lawrence Bragg determined the unit cell parameters from the Laue diagrams of zinc blende[58]. Subsequently, he carried out the complete structure determination of several inorganic salts including NaCl and KI[59].

1.2.1 Basics of crystallography

The definition of crystal given by the International Union of Crystallography is "A material is a crystal if it has essentially a sharp diffraction pattern. The words essentially mean that most of the

diffraction is concentrated in the relatively sharp Bragg peaks, besides the always present diffuse scattering".[60]

Symmetry operations

Symmetry is an important concept - the corner stone of many other concepts in crystallography. From Merriam-Webster dictionary, symmetry is defined as "the quality of something that has two sides or halves that are the same or very close in size, shape and position". In the field of crystallography, symmetry is very useful in classification, simplification and description of crystal structures as well as in the process of solving structures. If certain symmetry is present in the crystal structure, the structure can be perfectly superimposed with itself by following the corresponding symmetry operation. In three dimensional space, there are four kinds of simple symmetry operations- inversion, reflection, rotation and translation. Figure 1.10 demonstrates these four kinds of symmetry operations (inversion, reflection, rotation and translation) by using the author's hands. Both inversion and reflection operation change the chirality of the object while the rotation and translation do not. There are one, two, three, four and six-fold rotation symmetry operations meaning rotating 360°, 180°, 120°, 90° and 60°, respectively. There are more complex symmetry operations which combine the simple ones. As shown in Figure 1.10, the symmetry operations in the second row are composed of two operations listed in the first row.

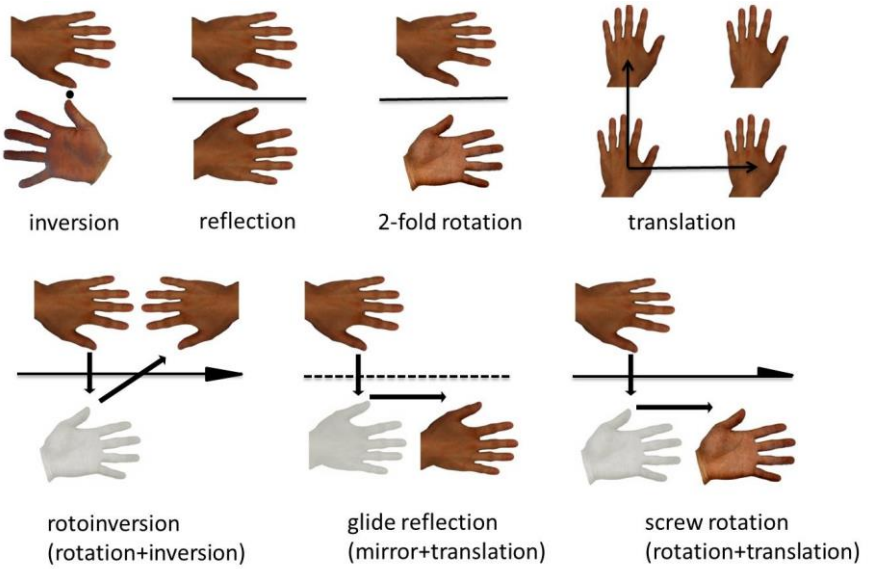

Figure 1.10 Illustration of symmetry operations

Unit cell and Bravais lattice

With the concept of symmetry in mind, we can classify all the structures into seven crystal systems[61] – triclinic, monoclinic, orthorhombic, tetragonal, trigonal, hexagonal and cubic. As shown in Table 8.1, there are minimum requirements for each crystal system. For instance, the orthorhombic crystal system requires the crystal to have reflection or rotation symmetry operations along three different directions. To fulfill this requirement, the normal axes of the reflection planes have to be perpendicular to each other.

Crystal structure describes the number and kinds of atoms as well as how the atoms are arranged in a crystal. The crystal structure can be described by using the unit cell which repeats throughout the crystal by translation operations along the directions of three axes (except for the aperiodic crystals; the concepts mentioned in this thesis will be referred to the periodic crystals only). The unit cell can be imagined to be a three dimensional parallelepiped which is a very small sized representative of the whole structure. The crystal is composed of millions of these parallelepipeds placed one by one in space. The unit cell can be defined by using the lengths of the three independent edges and the three angles between each two edges. The lengths of the edges are denoted by *a*, *b* and *c*; the angles between them are denoted by α (angle between *b* and *c*), β (angle between *a* and *c*) and γ (angle between *a* and *b*). The shape and size of the unit cell are not chosen arbitrarily but according to the symmetry of the structure.

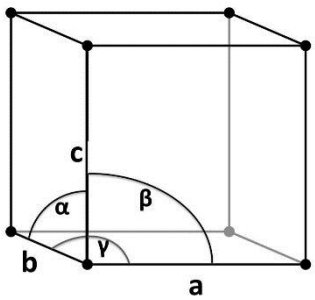

Figure 1.11 Illustration of unit cell and unit cell parameters

Bravais lattice is a concept that describes the translation symmetry of the whole structure. The Bravais lattice is a mathematic term which means an array of identical discrete points arranged in a periodic way. The array can be generated from the point at the origin and the translation operations with three basic vectors. A crystal structure can

be related to its Bravais lattice by considering the lattice point as an atom or a group of atoms. There are primitive and centred Bravais lattices. For the former one, all lattice points fall on the vertex of the unit cell and each lattice point represents all the atoms in the unit cell. While for the later one there are extra lattice points falling on the body center, face center or the other special positions of the unit cell. In this case, the lattice point only represents part (1/2, 1/3 or 1/4) of the unit cell.

The unit cell parameters and Bravais lattice follow different rules for crystals in different crystal systems (Table 8.1 lists the requirements for each crystal system). For instance, for crystals in cubic systems, the lengths of all axes must be equal and all angles must be equal to 90°. But it doesn't mean that a crystal with unit cell parameters obeying these rules has to be in the cubic crystal system. The crystal system can only be determined from the symmetries.

The concept of trigonal and hexagonal crystal systems as well as rhombohedral and hexagonal Bravais lattices should be distinguished. As shown in Table 8.1, a structure in the hexagonal crystal system has a 6-fold rotation symmetry and can be abstracted into a hexagonal Bravais lattice. A structure in the trigonal crystal system has only 3-fold rotation symmetry, but when simplifying it into a Bravais lattice, either a primitive hexagonal or rhombohedral lattice can be obtained.

Space group

Now we can divide all structures into 7 crystal systems or 14 bravais lattices. However, there are still big differences in symmetries of crystals within one class. Space groups are the symmetry groups of 3-dimensional crystal structures. 230 space groups describe all the possible groups of symmetry operations[61].

The space groups are often notated by using international short symbols. The international short symbol of a space group always starts with a letter P, A, B, C, I, or F, representing the centering type of the Bravais lattice. The meaning of the second, third and fourth positions vary depending on the crystal system. The symbol of a triclinic crystal system is either P1 or $P\bar{1}$. The symbols of space groups in the monoclinic crystal system are always simplified into 1 or 2 letters (or numbers). The second position refers to the symmetry operations relative to the unique (often taken as b-axis) direction which are limited to the 2-fold rotation, mirror or related symmetry operations. For

orthorhombic crystals, the last three positions refer to the symmetry operations relative to the a, b, and c-axis directions, which are restricted to be the 2-fold rotation, mirror or related symmetry operations. Space group symbols of tetragonal crystals can have two positions or four positions. The second position referring to the symmetry relative to the c-axis direction should be a 4-fold rotation or related symmetry operations. For the symbols of trigonal space groups, at the first one of the 3 positions there should be 3 or $\bar{3}$, while for the hexagonal ones, there should be 6 or $\bar{6}$. Cubic crystals have the highest symmetry. There are 4 positions in the space group symbol (some have only 3) among which the second one should be 3 or $\bar{3}$ indicating the 3-fold rotation along the body diagonal direction.

1.2.2 X-ray diffraction

The distance between neighboring atoms in solids is within a few Å. The resolution of any imaging system is theoretically limited by the wavelength of the radiation (visible light, X-rays, electrons or neutrons). According to the classic Rayleigh criterion, two points can be distinguished if the maximum of one point is at least at the first minimum of the other point.[62] The theoretical resolution limit of any imaging system can be expressed as

$$R = \frac{0.61\lambda}{\mu \cdot \sin\beta} \qquad (1.1)^{62}$$

In equation 1.1, R is the spacial resolution, λ is the wavelength of the radiation, μ is refractive index of the viewing medium and β is the collection semi-angle of the magnification lens. Although μ ·sinβ is related to the type of the microscope, we can give a simple approximation here. For a visible-light microscope, the typical μ×sinβ value is around 1, which means the resolution of the microscope is around half of the wavelength of the radiation (in the scale of a few hundred nm). This value is 3 orders of magnitude larger than the resolution required for atomic structure determination. A feasible solution is to use other radiation sources. X-rays have much shorter wavelength than visible light. X-rays from a copper target has the wavelength of 1.54 Å which is comparable to the atomic distance in solid materials. But X-rays can't be utilized in the same way as the visible light in light microscope, because the X-rays cannot be focused again to form an image. One of the major reasons is about the lens materials.[63] The transparent materials for manufacturing lens have

refractive indices substantially larger than 1 for visible light but slightly smaller than 1 for X-rays. Therefore in order to reveal atomic structures by X-rays, we need to replace the lens by mathematic methods.

Bragg diffraction

X-rays are electromagnetic waves with wavelengths in the range from 0.1 Å to 10 Å. The length is similar to the atomic distance in solid materials. Thus X-rays pass through a crystal along certain direction, Bragg diffraction occurs, resulting in sharp diffraction spots. Bragg's law is defined as

$$n\lambda = 2d \cdot sin\theta \qquad (1.2)^{64}$$

where *n* is an integer, λ is the wavelength of the electromagnetic wave, d is the distance between the atom layers and θ is the angle between incident beam and atom layer. Figure 1.12 illustrates how Bragg's law was derived. When X-rays are scattered by the atom layers denoted by black spots, the optical path difference of 2Δ is generated for the scattered beam. When 2Δ is equal to integer times of the wavelength of the radiation, the scattered beams from different layers reinforce each other to form strong diffraction peaks. Otherwise the scattered beams cancel each other in such directions. Therefore, when illuminating a crystal with X-rays, only incident beams from certain directions can generate strong diffraction peaks. If the directions of the incident beam and the scattered beam are recorded when diffraction peaks observed, the distance between the atom layers can be revealed by using the Bragg's law.

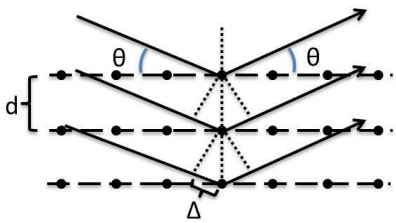

Figure 1.12 Illustration of Bragg's law.

Miller index and Bragg plane

The equation 1.2 can be rearranged into

$$\lambda = 2 \cdot \frac{d}{n} \cdot sin\theta \qquad (1.3).^{65}$$

Instead of thinking the optical path difference as integer times of the wavelength, we can imagine sets of parallel planes that have the inter-

planar distance of *d/n*. These sets of parallel planes are defined as Bragg planes. A miller index hkl is assigned to a set of parallel planes that cut the three axes at the points $\frac{n}{h}a, \frac{n}{k}b \; and \; \frac{n}{l}c$. The sets of planes are denoted as (hkl) and the inter-planar distances are denoted as d_{hkl}. Therefor Bragg's law can be rearranged to

$$\lambda = 2d_{hkl} \cdot sin\theta \qquad (1.4).^{65}$$

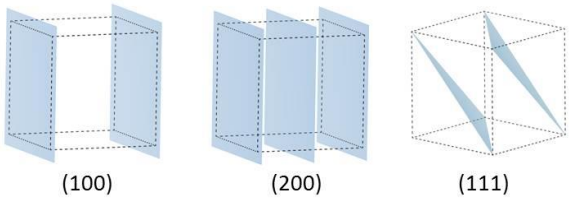

Figure 1.13 examples of Bragg planes in real space

Reciprocal space

Bragg's law helps us to understand the origin of diffraction spots, while the reciprocal lattice gives us a vivid feeling of diffraction patterns. As mentioned in chapter 1.2.1, crystal structures can be abstracted into Bravais lattices. A Bravais lattice in real space can be further transformed into a lattice in reciprocal space. This transformation is actually converting every set of Bragg planes in real space to a point in reciprocal space. The transformation from a Bravais lattice to a reciprocal lattice follows three equations.

$$a^* = \frac{b \times c}{V};\; b^* = \frac{c \times a}{V};\; c^* = \frac{a \times b}{V} \qquad (1.3)^{66}$$

In equation 1.3, *a**, *b** and *c** refer to the reciprocal lattice vectors, *a*, *b*, *c* refer to the Bravais lattice vectors and *V* refers to the volume of the unit cell.

The reciprocal lattice points can be represented by Miller indices as

$$g_{hkl} = ha^* + kb^* + lc^* \qquad (1.4).^{66}$$

There is an easy way to figure out the geometry of the reciprocal lattice from the Bravais lattice. The direction of g_{hkl} is normal to the corresponding Bragg plane (*hkl*), while the length of the g_{hkl} is equal to $\frac{1}{d_{hkl}}$.

Each Bragg plane can generate a diffraction spot when a certain incident angle is reached. The reciprocal lattice can be used to build up the physical picture of the geometry of these diffraction spots of the crystal. Each diffraction pattern is like a slice of the reciprocal lattice.

Ewald sphere

We discussed about the diffraction spots and reciprocal lattice. The Ewald sphere can give us a clear representation of the relation between them.[67]

From Bragg's law and the reciprocal lattice, we can derive the equation

$$|g_{hkl}| = \frac{1}{d_{hkl}} = \frac{2}{\lambda} \cdot sin\theta \qquad (1.5).$$

To visualize the equation, we can draw a sphere with diameter of $\frac{2}{\lambda}$ centered at the sample. The origin of the reciprocal lattice lies at the cross of the sphere and the extension line of the incident beam. If a lattice point coincides with the sphere, the Bragg diffraction condition of the corresponding Bragg plane is satisfied. Therefore there is diffracted beam along the direction from the center of the sample to the reciprocal lattice point *hkl*.

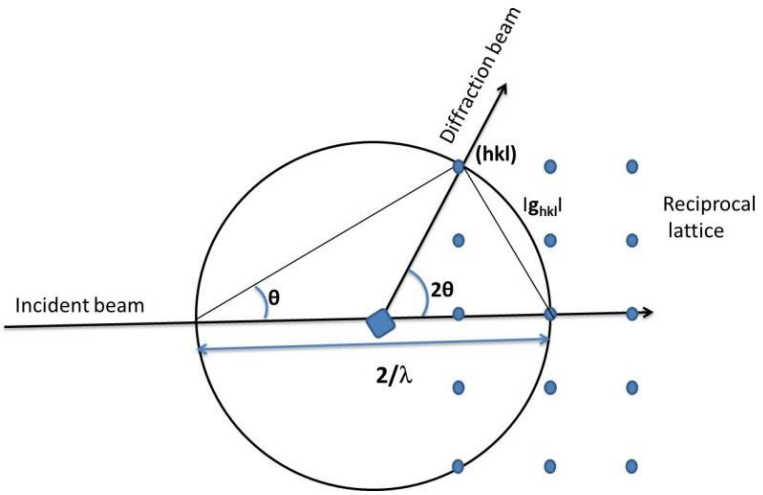

Figure 1.14 Illustration of the Ewald sphere

Fourier transform

The above discussions are about the geometry of the diffraction pattern. The intensity of the diffraction spots is another important type of information that we can obtain experimentally. The geometry of the diffraction pattern is determined by the size and shape of the unit cell while the intensities of the diffraction spots are determined by the types and positions of atoms within the unit cell. To relate the diffraction intensity with the crystal structure, we need the tool of discrete Fourier transform which is a mathematical method for the transformation of a

periodic function into a series of sinusoids.

Structure factor

Since atoms are arranged periodically in a crystal, the electron density map is also a periodic function of the coordinates (x, y, z). Therefore the density map of the crystal can be decomposed into a discrete series of complex sinusoids. These complex sinusoids are called the structure factor of the crystal.

$$F(h\,kl) = V \cdot \sum_{x,y,z} \rho(xyz) exp[2\pi i(hx + ky + lz)] \qquad (1.6)^{68}$$

In equation (1.6), *F(h, k, l)* is the structure factor, V is the volume of the unit cell, *ρ(x, y, z)* is the function of electron density map. Since the X-rays are scattered by only electrons, the scattering power is proportional to the electron density. The intensities of the complex sinusoids are related to the experimental intensity values of the reflections (Intensity $\propto |F_{hkl}|^2$).

The scattering power is also related to other factors including scattering angles, thermal vibration of each atom and the radiation wavelength. So *ρ(xyz)* in equation (1.6) should be replaced by $g_j\, t_j(\theta,\lambda) f_j(\theta,\lambda)$ where *j* refers to the *j*-th atom, g_j refers to the occupancy of the atom, $t_j(\theta,\lambda)$ refers to the atomic displacement parameters and $f_j(\theta,\lambda)$ refers to the atomic scattering factor. Furthermore, since the electrons are found mainly in small volumes around the atomic volumes, the electron density at position far from the atoms is almost zero. Considering these facts, the equation (1.6) can be changed to

$$F(hkl) = V \cdot \sum_j g_j \cdot t_j(\theta,\lambda) \cdot f_j(\theta,\lambda) \cdot exp\left[2\pi i(hx_j + ky_j + lz_j)\right] \qquad (1.7)^{65}$$

The electron density map can also be reconstructed from the structure factors (with both amplitudes and phases) by inverse Fourier transformation.

$$\rho(xyz) = \frac{1}{V} \cdot \sum_{hkl} F(hkl) exp[-2\pi i(hx + ky + lz)] \qquad (1.7)^{65}$$

The structure factors are complex sinusoidal functions which can be written in the format $F(hkl) = |F(hkl)| \cdot e^{i \cdot \emptyset(hkl)}$, where $|F(hkl)|$ means the amplitude and *Ø(hkl)* is the phase of the structure factor.

Friedel's law states that the structure factors of the reflections *h, k, l* and $\bar{h}, \bar{k}, \bar{l}$ have the same amplitude but opposite phases. With the Friedel's law, the equation can be simplified into a summation of a series of cosine functions.

$$\rho(xyz) = \frac{1}{V} \cdot \sum_{hkl} |F(hkl)| \cdot cos[2\pi(hx + ky + lz) - \emptyset(hkl)] \qquad (1.8)^{69}$$

The above description is the mathematic expression of structure factors. There is an easier way to have a vivid feeling of the structure factors. Every structure factor can be seen as a cosine wave. If we imagine the value of the wave function represents the electron density, the electron density map can be drawn when we sum up all the structure factors - the waves, in real space. The direction of the wave is perpendicular to the corresponding the Bragg planes, the periodicity is the d_{hkl} values of Bragg planes and the amplitude is the absolute value of the structure factor. The origin of the wave can be known from the phase part of the structure factor. Therefore, the crystal structure including information of types and positions of atoms can be reconstructed by using the structure factors.

1.2.3 Electron diffraction

We mentioned in the previous part that X-rays have the advantage of short wavelengths which can be utilized for resolving the atomic structures. Electrons have even shorter wavelengths than X-ray. Electrons are particles and at the same time waves. The wavelength of electrons depends on the velocity and can be manipulated by accelerating the electrons. With a 200 kV accelerating voltage, the wavelength of electrons is as short as 0.025 Å.

Diffraction patterns can also be obtained by using electrons as the radiation source. However, the way electrons interact with mater is different from X-rays. Unlike x-rays which only interact with electrons of the atoms, electrons interact with the electric field which related to both the negatively charged electrons and positively charged nuclei. Because of the different interaction mechanisms, the expression for structure factor in electron diffraction is different from the one for X-ray diffraction.

$$F(hkl) = \frac{\sigma \cdot V}{\lambda} \sum_{xyz} \varphi(xyz) \cdot exp[2\pi i(hx + ky + lz)] \qquad (1.9)^{70}$$

$$\sigma = \frac{2\pi m_e \lambda}{h^2} \qquad (1.10)$$

In equation 1.9 and 1.10, $\varphi(xyz)$ is the electrostatic potential, m_e is the electron mass, h is the Planck's constant. The amplitude of this structure factor is also related to the intensity of the reflection.

Similar to X-ray diffraction, we can reconstruct the electrostatic potential map by inverse Fourier transformation of the structure factors.

$$\varphi(r) = \frac{\lambda}{\sigma \cdot V} \sum_{hkl} F(hkl) \cdot exp[-2\pi i(hx + ky + lz)] \qquad (1.11)^{70}$$

1.3 Objectives and contents of this thesis

This work includes two parts – synthesis and structure characterization. Although the synthesis is a minor part in the thesis, we aimed to obtain some hints on effects of different reagents on the final products in zeolite synthesis. Optimizing of the synthesis gel resulted in single crystals of zeolite ITQ-33.

The second part is about the structure characterization. Since crystal structures determine many important properties of open-framework materials, this work is aimed to apply different methods to determine the structure of such kind of materials from SXRD and PXRD data.
In the chapter 2, the basic knowledge of SXRD and PXRD as well as the popular structure solution method is described.
For the disordered and twinning structures, it is difficult to obtain satisfactory result even from good SXRD data. In the chapter 3, we gave two examples about structure determination of disorder and pseudo-merohedric twinning respectively.

Solving complicated crystal structures from PXRD still need lots of expertise and experiences. In the chapter 4, we gave examples on structure determining for both inorganic framework and MOF materials. We hope that this thesis can provide some useful experiences and be inspiring to those who work in the field of synthesis and structure determination of framework materials.

2 Synthesis and structure characterization using diffraction methods

2.1 Synthesis of zeolites

Synthesis of zeolites is mostly done in the hydrothermal condition or ionothermal conditions (by using ionic liquid as solvent).[71] Although zeolites with over 200 framework types have been discovered or synthesized, it is still very difficult to predict and design the synthesis of zeolites. The trial and error methods assisted with empirical knowledge is the main stream in the field of zeolite synthesis.

General route of zeolite synthesis

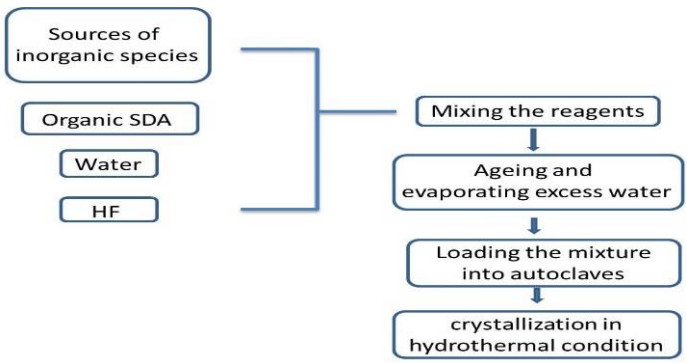

Figure 2.1 Zeolites synthesis route which was employed in this work.

In this thesis, synthesis of zeolites was carried out following the route shown in Figure 2.1. The sources of inorganic species include tetraethyl orthosilicate (TESO), germanium dioxide, aluminum isopropoxide and boric acid. Typically, the sources of inorganic species were dissolved in the solution of SDA under stirring. The mixture was then stirred overnight before hydrofluoric acid (or ammonium fluoride solution) was added to the solution. The mixture was then placed in the oven of 50 ^{o}C to evaporate the excessive water. In the case that the

sample was over dried (water left in the sample is less than the desired amount), water was added by using micropipette to reach the desired composition. Then the mixture was loaded into a Teflon lined autoclave and placed into the oven.

Synthesis condition of ITQ-33

The organic SDA used to synthesize the single crystals of ITQ-33 is 1-butyl-3-methylimidazollium hydroxide. Although a similar compound, 1,2-dibutyl-3-methylimidazolium hydroxide was synthesized and tried as the SDA, the crystal obtained is smaller in size than the one synthesized by using the former SDA.

(a)

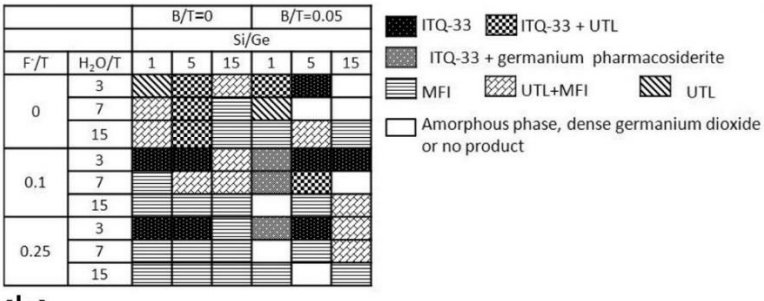

(b)

	H_2O/T	App.	F^-/T	App.	Si/Ge	App.	B/T	App.
ITQ-33	3	12		5	1	6	0	7
	7	3	0.1	7	5	9	0.05	9
	15	1	0.25	4	15	1		
ULT	3	6	0	10	1	4	0	10
	7	6	0.1	5	5	6	0.05	7
	15	3	0.25	2	15	6		
MFI	3	4	0	8	1	8	0	19
	7	10	0.1	9	5	7	0.05	10
	15	15	0.25	12	15	14		

Figure 2.2 (a) the diagram of composition of synthesis gel and corresponding products; (b) the effect of each reagent on appearance times of each phase in the products. (T: T-atoms, App.: the appearance times of certain product in certain condition)

Figure 2.2(a) shows the synthesis diagram of ITQ-33. The crystallization was carried out at 180 ^oC for 6 days. The different compositions of the synthesis gels resulted in different products

including ITQ-33, a ULT type zeolite, an MFI type zeolite, some dense crystalline phases (germanium pharmacosidertie, germanium dioxide) and amorphous gel.

From the synthesis diagram, it was observed that the appearances of different types of zeolites follow certain rules. For ITQ-33, with the decrease of water/T ratio, ITQ-33 appears in the products much more frequently. In addition, it is difficult to synthesize ITQ-33 from the starting compositions with high Si/Ge ratio (15). For the UTL type zeolite, the F^-/T ratio is the key factor in the synthesis. The increase of the F^-/T ratio significantly reduces the appearance frequency of UTL type zeolite. For the MFI type zeolite, it shows strong tendency toward the synthesis conditions with higher H_2O/T ratio and less framework substitution atoms (Ge, B).

2.2 Diffraction methods

Various methods can be used for structure characterization. In this thesis, we use mostly three methods – single crystal X-ray diffraction (SXRD), powder X-ray diffraction (PXRD) and rotation electron diffraction (RED) in a transmission electron microscope. There are advantages and disadvantages for each methods. Hence for crystals with different nature, appropriate method should be chosen.

Table 2.1. The features of three different methods[72].

	SXRD	PXRD	RED
Required crystal size	Large (≥5μm)	Small (≥50nm)	Very small (≥a few nm)
Peak overlapping	No	Yes	No
Data completeness	High	High	Moderate
Intensity	Kinematical	Kinematical	Dynamical
Unit cell determination	Easy	Difficult	Easy
Symmetry determination	Easy	Difficult	Easy
Structure determination	Easy	Difficult	Easy

2.3 Single crystal X-ray diffraction

SXRD can be applied to samples with crystal sizes larger than 5 μm. For most cases, it is routine work to collect data, reduce data, solve and refine the crystal structure. The results from SXRD show high accuracy on the atomic positions, occupancy and even charge density maps[73]. It

is also possible to reveal details in the structures e.g. disorder and twinning [74].

Instrument and basic principles

Single crystal X-ray diffractometer is composed of three major parts – X-ray source, sample stage and detector. The X-ray source can be an X-ray tube in a laboratory diffractometer or synchrotron light source. For the X-ray tube, an electron beam hits the metal anode e.g. copper, molybdenum metal, which generates characteristic radiation. After going through a filter and monochromator, X-rays with a certain wavelength (1.5406 Å for copper Kα1 and 0.7093 Å for molybdenum Kα1) is used to illuminate the sample and generate diffraction patterns. The synchrotron light source utilizes the radiation generated by changing the moving direction of high-speed electrons. X-rays from synchrotron light source have much higher intensity compared to the X-ray tube and thus the minimum crystal size required is much smaller. The sample stage controls the rotation of the crystal. As discussed above, only when the reciprocal lattice points coincide with the Ewald sphere, will there be Bragg diffractions. During the measurement, the rotation of the crystal drives the reciprocal lattice to cut the Ewald sphere and cause diffractions. The detector records the positions and intensities of the diffraction spots. At the same time, a computer also records the orientation of the crystal. From both of these information, the reciprocal lattice can be reconstructed. Figure 3.1(b) shows the general procedure for determining the atomic structure of a crystal from SXRD.

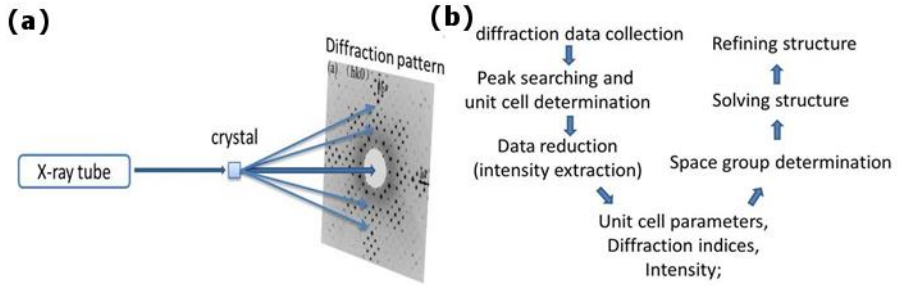

Figure 2.3 Scheme of single crystal XRD and general procedure of solving and refining crystal structures from SXRD data.

Direct methods

The geometry of the reciprocal lattice and the amplitudes of structure factors can be measured directly by SXRD. But the structure factor

phases are lost during the measurement when the diffracted beams are recorded by the detector. Without the phase information, we can not reconstruct the atomic structure of the crystal by using inverse Fourier transform. Direct methods are one of the most famous methods for tackling the phase problem.

There are about 15000 reflections in the resolution range from infinite large to 1 Å for a crystal structure with a unit cell volume of around 5000 $Å^3$. But there are only a few hundred atoms (around 250 non-hydrogen atoms for crystals of organic compounds) in the unit cell. If we consider every reflection is independent, there is obvious excessive information. Hence there must be some relations among the different reflections.

Firstly, we can utilize the symmetry of the crystals to exploit the relations between the reflections. The reflections in reciprocal space show similar symmetry as the structures in the real space structure. For the symmetry-related reflections, the intensities are supposed to be the same and the phases follow the equation (3.1)

$$\emptyset(h_2k_2l_2) = \emptyset(h_1k_1l_1) - 360^o \cdot (h_1t_x + k_1t_y + l_1t_z) \qquad (3.1)$$

Where $h_1k_1l_1$ and $h_2k_2l_2$ are two symmetry related reflections, $\emptyset(hkl)$ is the phase of the reflection and (t_x t_y t_z) is the translation vector of the corresponding symmetry operation.

Secondly, we can also make use of our chemistry knowledge. The electron density is positive at some discrete sites (atom positions) spreading more or less evenly throughout the unit cell. The electron density is close to zero at the places other than the atom positions but never goes to negative. Based on these facts, the triplet relation can be derived. It states that if the sum of the indices of three strong reflections is zero, the sum of the phases is probably equal to zero too. The triplet relation can be summarized by equation (3.2)

$$\emptyset(h_3k_3l_3) = 360^o - \emptyset(h_2k_2l_2) - \emptyset(h_1k_1l_1)$$
$$\text{While} \quad (h_3k_3l_3) + (h_2k_2l_2) + (h_1k_1l_1) = 0 \qquad (3.2)$$

By using these two kinds of relations, the number of phase needed to be determined can be reduced.

Direct methods are based on these two relations. The general procedure for direct methods is as follows.[70]

1. Before solving a structure by direct methods, the unit cell and symmetry of the structure are predicted from the geometry of the reflections, intensity distribution and the reflection conditions. The symmetry related reflections are combined.

2. The amplitudes of all reflections are normalized to compensate for the effects of systematic enhancement of reflections and differences on scattering power at different angles.
3. To fix the origin of the unit cell, the phases of a few strong reflections are fixed.
4. A group of reflections is selected based on two criteria: those with the strongest normalized intensities and those can generate most triplets.
5. All possible combinations of phases are assigned to this group of reflections, e.g. for centrosymmetric structures, 0^o, 180^o are the only two choices; for non-centrosymmetric structures, more choices were made available e.g. 45^o, 135^o, 225^o and 315^o. By using triplet relations, as many as possible strong reflections are phased.
6. The phasing results from all these possible combinations are refined by employing tangent formula and sorted by using a figure of merit.
7. Electron density map is calculated by using several groups of phases with highest figure of merit and corresponding reflection amplitudes. Atoms are assigned at the positions of the peaks. An agreement factor is used to select the best structure model.

Structure refinement

After obtaining the initial structure model, a more interactive procedure is needed to complete the crystal structure. The process involves least-squares refinement of parameters e.g. atomic positions, occupancy and atomic displacement parameters. In addition, the difference electron density map is employed to locate the missing parts in the model. During the structure refinement, information of chemical knowledge is used to regulate the structure by constrains and restrains. Constrains are the mathematical method to reduce the number of parameters. Restrains are the method to drive the refining value to a target value by adding a penalty to the figure of merit used for the refinement.

Computer Programs

In this thesis, several computer programs were used for solving structures from SXRD data. The software package “Crysalis pro” was used in the data collection, reduction and absorption correction. The program “Xprep” was used to analyze the symmetry and statistics of the diffraction data. The program package “SHLEX-97” was used to solve and refine crystal structures.[75] The program “Platon” was used to treat the diffraction data for porous structures with disordered guest

molecules in the pores.

2.4 Powder X-ray diffraction

As described in Table 2.1, SXRD only works when crystals with sizes larger than 5 μm are available. However, in many cases, due to the nature of the crystals, limitations on synthesis conditions or other reasons, only small crystals are available. In such cases, PXRD can be used to determine crystal structures.

Instrument and basic principles

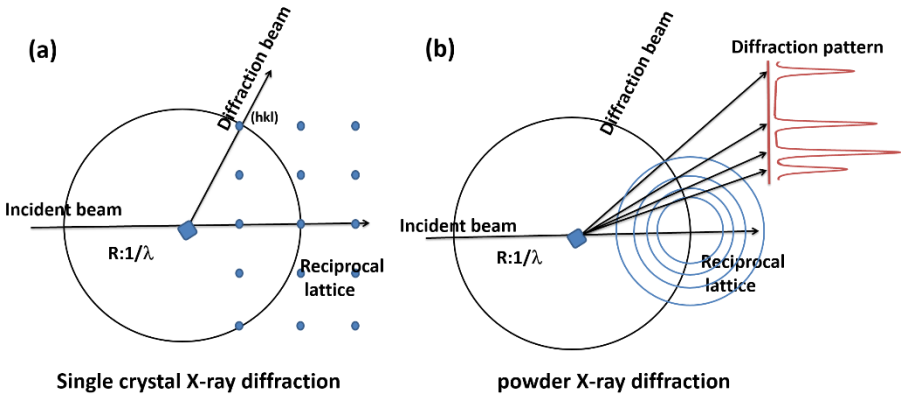

Figure 2.4 Comparision of the principles of SXRD and PXRD.

Figure 2.4 compares the working principles of SXRD and PXRD. For SXRD, only when the Ewald sphere coincides with reciprocal lattice points of the crystal can the Bragg condition be fulfilled and diffraction spots can be generated. For PXRD, we use a much larger amount of sample, which contains millions of crystals in random orientations. The reciprocal lattices of these crystals become spheres with different diameters rather than isolated spots. Therefore the Ewald sphere cuts every reciprocal sphere at once and generates all possible diffraction peaks. The underline reason is that there are crystals lying along every crystallographic orientation. When there is an incident X-ray beam, there are always crystals in just the right orientations for every Bragg peaks. Theoretically the diffraction peaks can be recorded at once if placing a detector covering the necessary angle range. In the synchrotron light sources, large planar detectors are used to collect data simultaneously at the same time to get good statistics of the data.

There are three major parts in a powder X-ray diffractometer – the X-ray tube, sample stage and the detector. Different from a single crystal X-ray diffractometer, in which the sample stage rotates about three axes to fulfill the Bragg conditions of all reflections in the resolution range, in powder X-ray diffraction, such rotation is not needed. However, in some cases, we still tilt and spin the sample during the measurement to have the correct optical path and to avoid possible preferred orientation.

Solving and refining crystal structure from PXRD

Solving and refining crystal structures from PXRD are more difficult than those from SXRD. The three-dimensional reciprocal lattice is compressed into a one-dimensional line. The pattern shows only the diffraction angles 2θ and corresponding intensity values. Therefore it is not surprising that there is overlapping of reflections. In fact overlapping of reflections is the major problem in structure determination from PXRD.

The general procedure for structure determination from PXRD is as follows.[76]

1. Index the powder pattern. Since the overlapping of reflections and the loss of the information about angles between pairs of reciprocal vectors, indexing of PXRD the pattern is one of the most difficult steps in the whole process.
2. Determine the space group of the structure from reflection conditions and assign intensities to reflections by decomposing the pattern. However this step may be different depending on the structure solution method.
3. Solve the crystal structure using reciprocal space methods, real space methods, dual-space methods or other methods.
4. Refine and complete the initial structure model with Rietveld refinement.

Structure solution methods

There are many methods developed for solving structures from PXRD data. In general, they can be classified into three kinds: reciprocal space methods, real space methods and dual-space methods. Reciprocal space methods include traditional direct methods, Patterson method and also other new methods e.g. maximum entropy and maximum likelihood methods.[77] The main feature of the reciprocal space methods is that the process involves the decomposition of

diffraction pattern, prediction of the structure factor phases in reciprocal space.

Real space methods are based on searching the structure in real space and evaluating the result by a figure of merit normally related to the difference between the calculated pattern and the observed pattern. These are the two important steps in real space methods. Different algorithms can be used for searching the structure, e.g. the Monte Carlo method, simulated annealing methods, and genetic algorithms.[78] There are also different ways of defining the figure of merit, for instance, bond lengths can be taken into account.

Duel-space methods are developing fast recently. The most famous example is the charge-flipping algorithm. It involves both the decomposition of the diffraction pattern, searching and changing the phase of the structure factors and modification of the electron density in real space.

The charge-flipping algorithm

The concept of the charge-flipping algorithm was proposed by Oszlânyi & Sütő[79] in 2004. The method was firstly used in SXRD to solve small molecule structures[80]. In 2006, Wu et al. solved a few simple crystal structures from powder XRD data by a method combining the repartitioning of peak intensity and the charge-flipping algorithm.[81] Later Baerlocher, McCusker & Palatinus adopted another approach for the repartitioning which considers the chemical information.[82] This method is very successful in solving structures from simple examples to complicated ones e.g. the ZSM-5 zeolite with the asymmetric unit containing 38 atoms and the unit cell containing 288 atoms. In the work of this thesis, a structure with 11 germanium atoms and 27 oxygen atoms in the asymmetric unit was solved by using the charge-flipping algorithm.

The principle behind the algorithm is relatively simple as shown in Figure 2.5. The pattern is decomposed and intensities are assigned to individual reflections before running the charge-flipping algorithm. To move toward the correct structure cycle by cycle, the method follows two clues reflection intensity and the fact that the real structure has positive electron density everywhere in the unit cell. The key step in the algorithm is the flipping of electron density where it is negative or smaller than a set value. Flipping of the intensity means over projecting of the intensity. It not only corrects the data as the other methods do but also it provide some extra energy to overcome local minimums.

Repartitioning of overlapping reflections is the other important step that gives rise to the success of the charge-flipping algorithm on solving structures from PXRD. Different methods have been applied to the repartitioning. Wu et al. applied a simple repartitioning method which divides the intensities based on the calculated structure factors of the present circle.[81] This interactive process helps to solve several structures from PXRD data. Baerlocher, McCusker & Palatinus adopted a more sophisticated repartitioning process which brings in extra information e.g. chemical composition, to avoid the closed circle of information.[82]

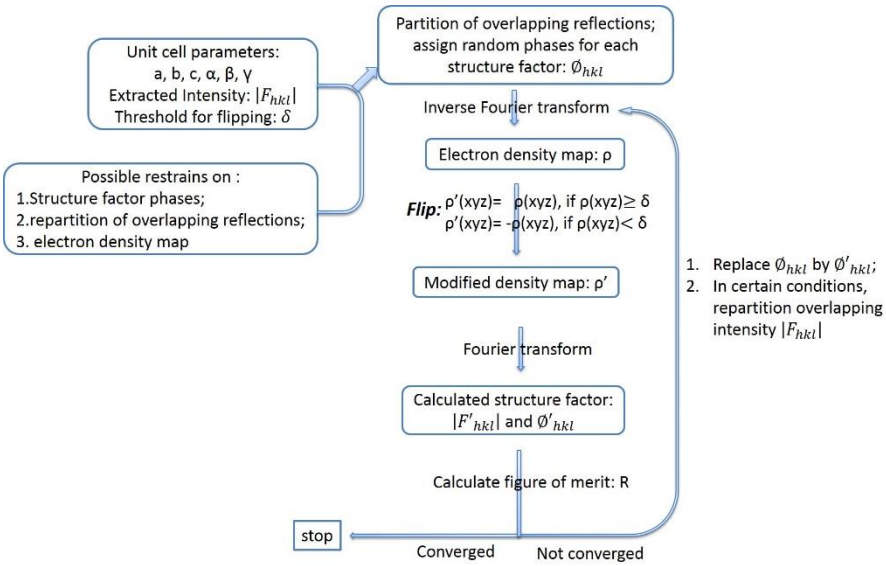

Figure 2.5 The flow chart of the charge flipping algorithm for powder XRD data.[82]

Computer programs

The program "X' Pert HighScore Plus" is used for PXRD pattern plotting and indexing. Several indexing methods were employed including "Treor", "ITO", "Dicvol04" and "McMaille". The program "Jana2006" and the program "TOPAS" were used for LeBail decomposition, intensity extraction and Reitveld refinement. The program "TOPAS" was also used for indexation and simulated annealing in some examples. Program "Superflip" was used to perform the charge-flipping algorithm.

2.5 Transmission electron microscopy

Transmission electron microscopy (TEM) uses electrons instead of X-rays as radiation. This results in some intrinsic differences between TEM and XRD. First of all, electrons interact more strongly with matter than X-rays do, which means electron diffraction can be applied to smaller crystals. Moreover, electrons can be precisely bent by electromagnetic lens. Therefore the diffracted electrons can be focused to produce images at atomic resolution.

Rotation electron diffraction

Since we can perform selected area electron diffraction (SAED) in a TEM, it should also be possible to perform SXRD-like experiments in the TEM. To collect 3D diffraction data, there are currently two methods: the automated diffraction tomography (ADT) method developed by Ult Kolb's group in Mazinz[83] and the rotation electron diffraction (RED) method developed by Xiaodong Zou's group in Stockholm[84]. In the ADT method, the whole 3D reciprocal space is scanned by utilizing precession electron diffraction to cover the space between two goniometer tilt positions. While the RED method resembles SXRD. The goniometer can be used to rotate the sample in the range from -70^o to +70^o, but the rotation is not precise enough. The beam tilt controlled by the lens is precise enough to sample the reciprocal space at a step of around 0.1^o and in the range of 2^o-4^o. By combining these two kinds of tilting, a series of electron diffraction patterns can be recorded in fine steps and in a wide tilt range.

The RED method is proved to be successful in solving a wide range of structures including zeolites, MOFs, COFs and so on.[85–87] Compared to XRD methods, RED method can be applied to smaller crystals. Moreover, RED method provides 3D diffraction data which avoids the peak overlapping. The diffraction data obtained from the RED method can be used in SXRD structure solution programs that are already well developed, e.g. SHELXS97 and SIR2014.

High resolution transmission electron microscopy

High resolution transmission electron microscopy (HRTEM) is another technique that can provide structural information. In simple words, an HRTEM image is the projection of the sample along a certain direction. However there are some factors that affect the contrast in the HRTEM images, e.g. the thickness of the sample and the focus condition. If a very thin crystal is imaged at the Scherzer focus

condition, the HRTEM image can be considered to represent the projection of electrostatic potential. The structure factors including both amplitudes and phases can be extracted from HRTEM images. Therefore, the HRTEM images from different directions can be used to reconstruct the structure.[88,89] Moreover, the structure factors from HRTEM can also be used as input information in structure solution process of PXRD.[90]

3 Disordered and twinned structures determined by using single crystal XRD

3.1 Disorder in extra-large pore zeolite ITQ-33 (paper I)

As mentioned in the introduction part, the pore structures of zeolites are crucial to their adsorption and catalytic behaviors. Therefore many researchers are focusing on searching for zeolites with novel structures, especially structures with extra-large pores (window size larger than 12-ring). The extra-large pores can enhance the mass diffuse rate inside the crystal, prolong the catalyst life time and change product selectivity in catalytic processes and enable zeolites to catalyze bulkier molecules.

In 2006, Corma's group in Valencia, Spain reported an extra-large pore zeolite with a 3D channel system. There are six structures that possess both extra-large rings and 3D channels. Among them, ITQ-43 (IRR), ITQ-44 (not available yet) and cloverite (CLO) are quite unstable after removal of SDA and ITQ-37(ITV) shows only limited stability after calcination. Zeolite ECR-34 (ETR) with 18×8×8 ring channel is quite stable but the 8 ring channel is too small for many catalytic reactions. ITQ-33 has 3D 18×10×10 channels showing better stability compared to the other extra-large pore zeolites mentioned above (except ECR-34). The catalytic test shows that ITQ-33 is a promising catalyst in the alkylation of benzene. It not only shows a longer life time, but also high selectivity on the desired product cumene, a widely used chemical.

Although the material receives much attention, there is still ambiguity on the structure of this zeolite. In the reported paper, the structure was solved and refined from PXRD data. Due to the relatively poor crystallinity of the material, the peak intensity decays very fast after the first peak, which makes it difficult to obtain detailed structure information.

Herein, we synthesized single crystals of ITQ-33 with sizes around 5 μm by using an imidazolium SDA. The crystals are still not big enough for most of the in-house diffractometers, hence SXRD data was

collected in the synchrotron light source Diamond which provides X-ray beams with much higher intensity.

Average structure

The structure was solved and refined with the program SHELXS97 and SHELXL97 respectively. The results suggest that the structure is similar to the one reported. It crystallizes in the space group *P*6/*mmm* with unit cell parameters of a = 19.3095 (5) Å, c = 11.513 (4) Å. There are four independent T atoms and eight independent oxygen atoms. As shown in Figure 3.1, the 3D interconnecting channels are composed of 10-ring channels along the crystallographic a and b-axes and 18-ring channels along the c-axis. We can describe the structure as clusters composed of three *mel* composite building units (CBU) connected through the 3-rings to form chains which are arranged in a honeycomb way and connected through double 4-ring (D4R) to form the 3D framework.

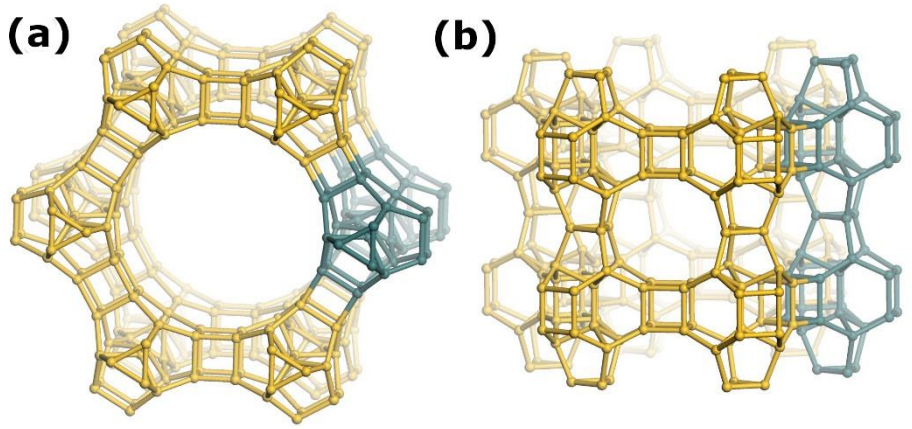

Figure 3.1 Average structure of ITQ-33 viewed (a) along the [001] direction; (b) along the [100] direction. A chain building unit is marked in cyan. Oxygen atoms are omitted to simplify the structure.

Revealing the disorder

Although the connectivity and the bond lengths of atoms are reasonable, the structure doesn't fit the diffraction data well. The best R1 value can be reached is 0.164 which is far from the acceptable level. The abnormal R1 value implies serious errors in the structure model.

Some missing atoms can be found by analyzing the residual peaks in the Fourier difference map. The strongest peak in the residual map has the intensity of 9 electrons per $Å^3$. After adding this peak into the structure model, an extra D4R appeared between the chains as shown

in Figure 3.2(b). The new D4R is $\frac{1}{2}c$ away from the D4R in the initial model. It bonds to the neighboring T atoms with reasonable bond lengths and angles. Therefore, the new D4R was considered as a disorder part of the one in the initial model. Refinement on this modified structure model resulted in another two residual peaks. These two peaks locate at the position $\frac{1}{2}c$ away from the T3 and T4 atoms. As shown in Figure 3.2(c), if we connect the new found atoms and T2 atoms, another framework could be found by shifting half of the unit cell from the initial structure model along the *c*-axis.

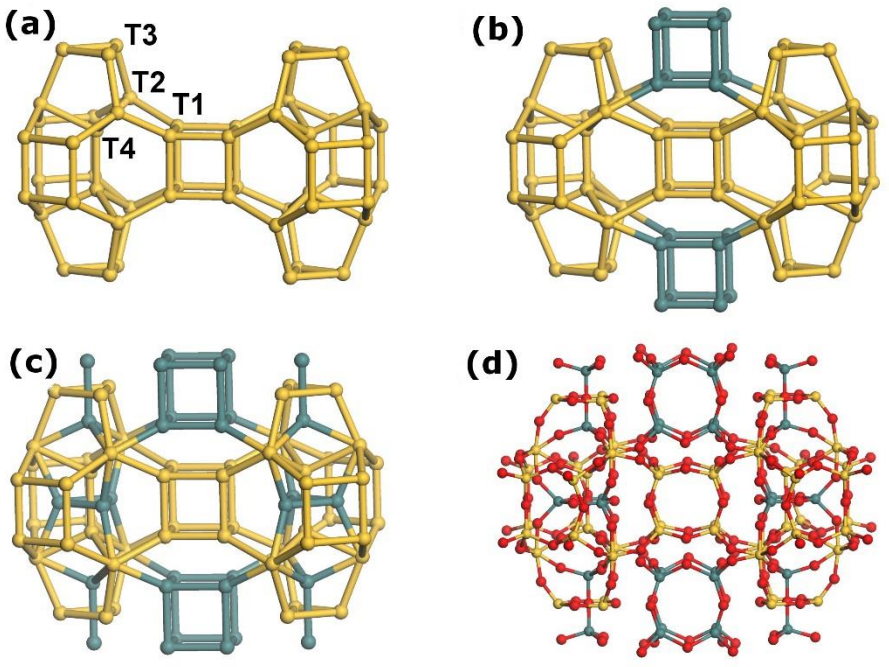

Figure 3.2 Structure models of different refinement stages. (a)the initial model; (b)the model after adding one residual peak; (c) the model with three residual peaks included; (d)the final model. Oxygen atoms are omitted in the first three models.

With the above clue, the structure was suspected to be split into two disordered parts at different heights along the *c*-axis. The T2 atoms are shared in both parts. Refining this structure model resulted in much better figures of merit than the initial model. Table 3.1 shows the refinement results of the initial and final structure models. Moreover, when refining the initial model, restrains on occupancies of atoms were needed to keep the refined occupancies positive. While with the final model, such restrains were not necessary. These facts imply that the later one should be a better description of the real material.

Table 3.1 Refinement figures of merit of the initial model without disorder and the final model with two disordered parts.

	Initial model	Final model
*R*int	9.58%	9.58%
*R*1	16.46%	6.69%
*wR*2	43.25%	22.17%
GOF	1.987	1.149

Cause of the disorder

After carefully examining the final structure of ITQ-33, it was found that the intrinsic structure feature enables such kind of disorder. As shown in Figure 3.3(a), the D4R is the bridge between two chain building units through connecting to the T2 atoms. Both the distances between T2(1)-T2(2) and T2(2)-T2(3) are 5.57 Å which is a suitable distance for connecting D4Rs. Therefore there are two possible positions for the D4R, which consequently give rise to the disorder in the structure.

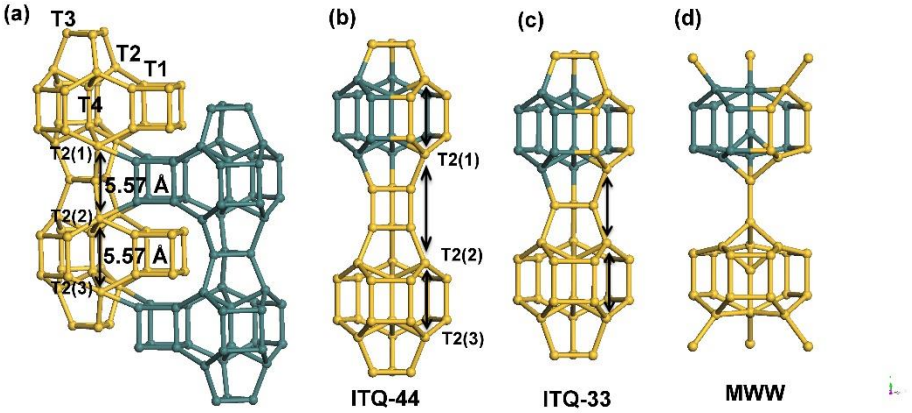

Figure 3.3 Structure of the (a) conjunction area of two disordered part; (b) chain building unit in ITQ-44; (c) chain building unit in ITQ-33; (d) building unit of MWW zeolite.

There are other structures in the zeolite database containing the *mel* CBU (shown in Figure 3.3). But none of them shows similar disorder phenomenon as ITQ-33 does. The structure of ITQ-44 is very similar to that of ITQ-33 except for that the 3-ring units are replaced by double 3-ring (D3R) units. This change increases the T2(1)-T2(2) distance but does not affect the T2(2)-T2(3) distance. Therefore there is only one possible position left for D4R, which rules out the disorder. MWW is built up from distorted *mel* CBU. The upper size and bottom size are

not symmetric, which makes the disorder impossible.

Understanding the disorder

Twinning and disorder occur frequently in crystals. The two concepts are closely related but quite different. Twins are regular aggregates of crystals consisting of the same species attached together in certain mutual orientation. For twining, the components shall be related to each other through a certain rotation, reflection or inversion operation. Each component should be with a sufficient size, which is usually much larger than 100 Å in any dimension. While disorder refers to a violation of the crystal symmetry and periodicity whose domain size is within a few unit cells.

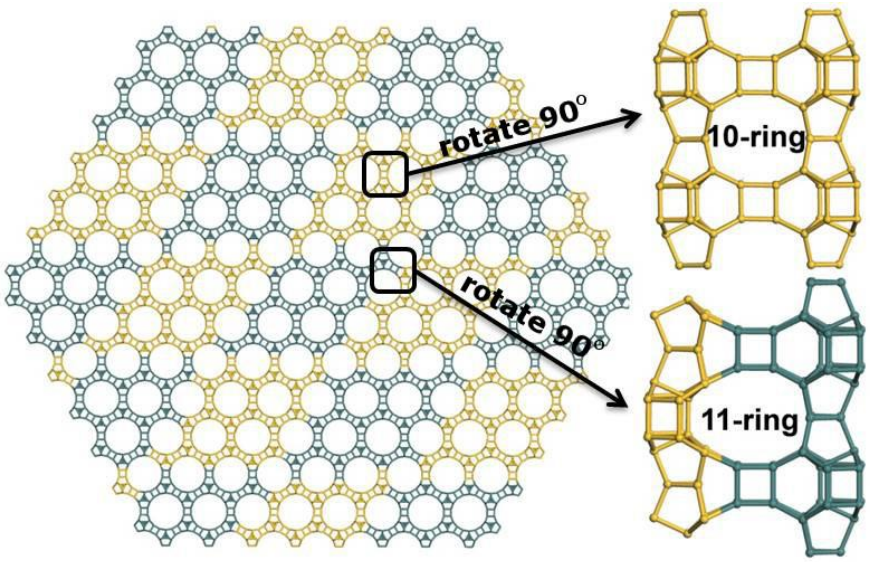

Figure 3.4 The proposed model of the real ITQ-33 crystal. The regions marked by two different colors refer to the two disorder parts.

Since only translation operation is involved in the ITQ-33 crystal, the phenomenon should be considered as disorder. From the thermodynamic point of view, the two parts are energetically equal and thus they are supposed to have the same proportion in the crystal. However, proportions of the two parts were refined to 10% for one and 90% for the other. In fact the refined proportion strongly depends on the size of the domain. With the increase of the domain size, the effect of disorder weakens sharply. Therefore, it is believed that the refined proportions of two parts reflect the size of the domain. We tried to study the domain size by using high-resolution transmission electron

microscopy (HRTEM), however the material doesn't survive long enough under high doses of electrons. More study is needed to reveal the domain size.

Figure 3.4 shows the illustration of the real ITQ-33 crystal. The domain size was drawn arbitrarily. It is worth mentioning that the pore size is different inside the domain and at the boundary. There are 10-ring channels perpendicular to the *c*-axis inside each domain but at the boundary it forms 11-ring windows which are very rare in zeolite.

Effect of Si/Ge ration on the Morphology

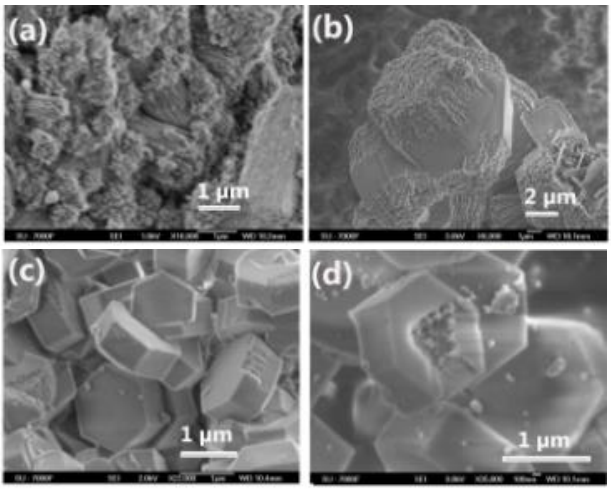

Figure 3.5 The changes of crystal morphology depending on the Si/Ge ratio in the synthesis gel.

The morphology of crystals changes upon the changes of the Si/Ge ratio in synthesis gel as shown in Figure 3.5. For Si/Ge = 5, fiber-like crystals were obtained. Increasing the Ge ratio in synthesis gel to Si/Ge = 2 produces bulker crystals but with a large amount of defects. When Si/Ge = 1, crystals in hexagonal shape with clear edges and corners were obtained. It is obvious that the Ge amount has significant effect on the morphology of crystals. From the refinement result, the majority of the Ge were located on the D4Rs. It is also a well-accepted observation that Ge facilitates the formation of the D4Rs in zeolite synthesis. At the condition of lacking Ge, crystals grow fast along the direction of the chain building unit but slowly along the perpendicular directions. Increasing the Ge amount can promote the chains to be connected.

Code for the embedded topology

After the detailed disorder in ITQ-33 structure has been clarified, the Structure Commission of International Zeolite Association (IZA) approved the framework type of ITQ-33 to be ITT. Detailed information can be found on website: http://izasc.fos.su.se/.

Conclusions

We synthesized single crystals of ITQ-33 and collected the SXRD data. It was found that ITQ-33 structure splits into two disordered parts in which one is $\frac{1}{2}c$ away from the other. This disorder is caused by the special structure feature of the column building unit. It provides two possible positions with equal possibilities to connect D4R units. This disorder also causes the change of the pore sizes. The 10-ring pores of the ordered structure transform to 11-ring pores at the boundary of two disordered domains.

3.2 Method for solving structure of a Pseudo-merohedric twinned crystal (paper II)

As described in the last section, the domains in the ITQ-33 crystals are related by a translation operation. The twinning are also quite common in framework materials e.g. ASU-21[91], which might induce obstacles in structure determination process. In this section we are going to introduce a method to solve structures when the domains are related by rotation operations.

Common methods for solving the twinning problem

With the rapid development on diffractometer, software and computation power, structure determination from SXRD data becomes kind of semi-automatic work in many cases. However, when a reasonable solution is not given out from the programs, the manual input from crystallographers becomes critical.

The symmetry of the crystal needs to be known before applying direct methods. The space group or a few closely related space groups can be picked out by examining the reflection conditions, symmetry of diffraction patterns and statistic values. However the imperfectness of the crystal like twinning/disorder can mislead us to a wrong space group. For instance, reflections from different components overlap with each

other in the merohedric or pseudo-merohedric twined crystals, which can lead to a higher symmetry in diffraction patterns. The most common way is to try all the subgroups of the current space group. In some complicated cases, the real space group is not even in the subgroup.
In this section we use a new and rational method to search for the real space group for a pseudo-merohedric twinned crystal. In addition, we show that the domain size has effects on the refinement results.

Initial structure solution

SXRD data of a crystal of [3Fe2S] complex with (cis-1,2-bis(diphenylphosphanyl)-ethene (dppv)) ligands was collected on a in-house X-ray diffractometer with Mo radiation source and a saffhire-3 CCD. The data was reduced and corrected by using program "CrysAlisPro", "X-shape" and "X-RED".

Bravais lattice with tetragonal unit cell was obtained with $a = b =$ 17.5833 (5) Å, c = 20.0333 (9) Å and $\alpha = \beta = \lambda = 90^{o}$. The intensity distribution of the reflections in pattern (hk0) shows a 4-fold rotation symmetry, which is consistent with the tetragonal crystal system. From the reflection conditions, a 4_2-screw axis along the c-axis and a n-glide perpendicular to the c-axis can be confirmed. However the reflection conditions of hhl: l=2n and $h\bar{h}l$: l=2n refer to a c-glides perpendicular to the a+b and a-b directions are ambiguous. 300 out of the 2055 expected absent reflections appear with intensities larger than 3σ. Thus two space groups $P4_2/n$ and $P4_2/nmc$ were picked out, one with c-glide plane and one without c-glide plane.

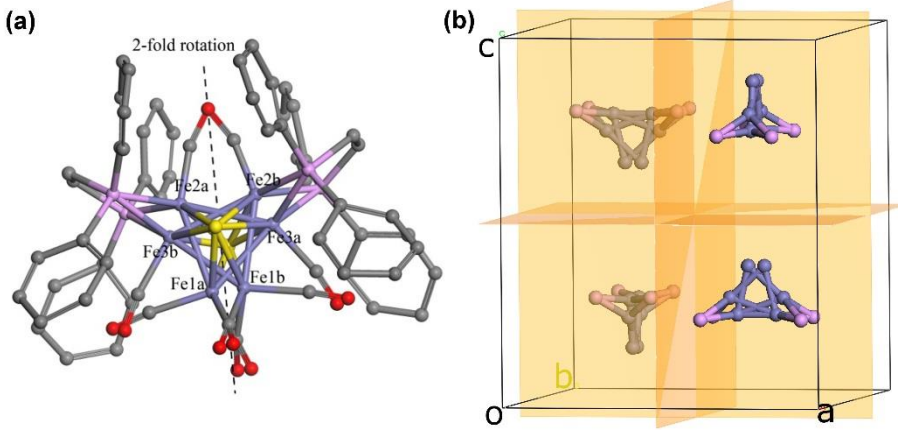

Figure 3.6 Initial structure model.(a) The detailed structure of the molecule; (b) the packing of molecules in the unit cell. Carbon, oxygen and iron atoms are omitted in (b) to simplify the illustration.

The structure solved in space group $P4_2/n$ by using SHELXS97 is shown in Figure 3.6. Although the structure was solved in $P4_2/n$, it shows the symmetry of $P4_2/nmc$. In the unit cell, there are four molecules. A 2-fold rotation axis goes though the molecule and forces part of the molecule to split into two disorder groups.

The figure of merit obtained (R1=0.179 for $I_{hkl} \geq 4\sigma$) are significantly poorer than the normal value. Considering the poor figure of merit and severe disorder imposed by the symmetry, we can conclude that there must be some errors in the space group.

Searching for space group

To search for the real space group, the normal method is to try different subgroups of the current space group. Here we search for it from the initial structure model instead.

As shown in Figure 3.6, the Fe atoms split into two triangles Fe1a-Fe2a- Fe3a and Fe1b- Fe2b- Fe3b. Since they are related by the 2-fold rotation axis, each of them has an occupancy of 0.5. If we believe that the splitting of atoms is due to the high symmetry imposed to the structure, the real structure can be obtained by removing the disordered groups for each molecule.

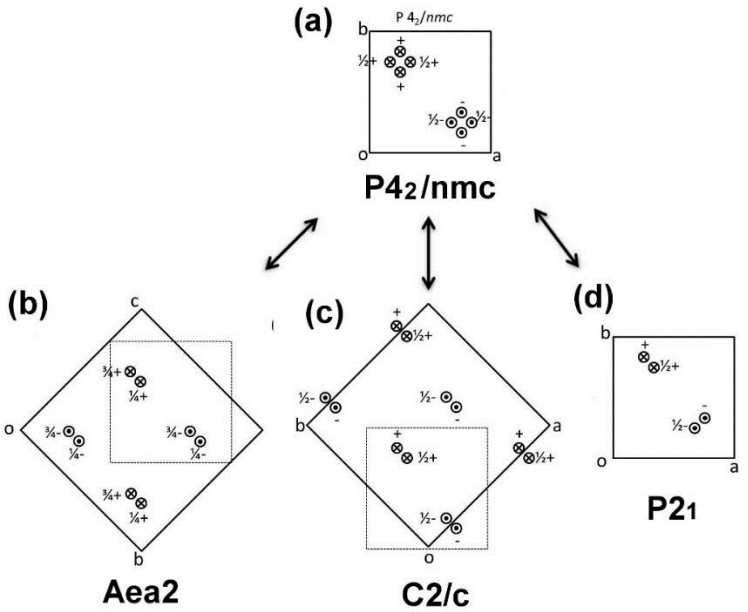

Figure 3.7 Illustration of space group transformation. The circles represent the iron atoms. The cross and dots inside the circles represent the two opposite orientations of the molecules.

Table 3.2 Reflection conditions and corresponding symmetry operation

	Reflection conditions		
exceptions[a]	initial unit cell[b]	transformed unit cell[c]	Symmetry elements
0/1334	*hk*0: *h*+*k* = 2*n*	0*kl*: *k* = 2*n*, *l* = 2*n*	*e*-glide plane
0/39	00*l*: l = 2*n*	*h*00: *h* = 2*n*	2_1-screw axis
300/2055	*hhl*: l = 2*n* $hh\bar{h}l$: l = 2*n*	*h*0*l*: *h* = 2*n* *hk*0: *h* = 2*n*	*a*-glide plane

a: the number of reflections that violates reflection conditions and the number of reflections expected to be absent;
b: unit cell of the initial structure model;
c: unit cell of the structure in the Aea2 space group;
d: 90° rotational twinning could cause the violation of the reflection conditions.

Since there are four molecules in the unit cell, there are 16 (2^4) possible choices. We can reduce half of the possibilities by fixing the choice of the first molecules because the rest can be generated from them. As illustrated in Figure 3.7, different ways of removing disordered groups can result in three different structures in space groups of *Aea*2, *C*2/*c* and *P*2_1 respectively. When we check the reflection conditions resulted by these structures, it was found that only *Aea*2 can fit the experimental data. Furthermore the ambiguous reflection conditions mentioned above can be well explained. If a pseudo-merohedric twin rotating 90° around the a-axis is added in the crystal, the positions of absent reflections (*h0l: h*=2*n*) can be partially covered by non-absent reflections from the other twin component, which caused the 300 reflections violating reflection conditions.

The finial structure model

Table 3.3 Figures of merit from the refinement with different structure models

Space group	***P*4$_2$/*n***	***Aea*2**	***Aea*2**
	disorder	twinning	disorder + twinning
$R1_{(I\geq 4\sigma)}$	0.178	0.117	0.072
*wR*2	0.462	0.320	0.178
GOOF	1.63	0.991	1.01

The unit cell was transformed from the initial cell to the unit cell (*a* = 20.033 Å, *b* = *c* = 24.867 Å) which is compatible to the space group *Aea*2. Correspondingly, the miller indices of reflections were also transformed. The structure in *Aea*2 was refined by considering 4 twin components which rotate n×90° around the common *a*-axis.
A rough refinement of the structure reduced the *R*1 value effectively from 0.178 to 0.117. In addition, the solvent and countering anions were located from the Fourier residual map. Further refinement resulted in

three distinguishable residual peaks of the disordered iron atoms. After adding them into the structure, the *R*1 value decreased to 0.072.

This result does not mean that there are both disorder and twinning in the crystal. Instead, similar to phenomenon in the ITQ-33 structure, this result is caused by the domain size. In a twined crystal, the domain size normally significantly large than 100 Å. But in the crystal with disorder, domain size is around a few unit cells. If the domain size fall into the range between these two, it is necessary to refine both of them simultaneously to achieve the best figures of merit.

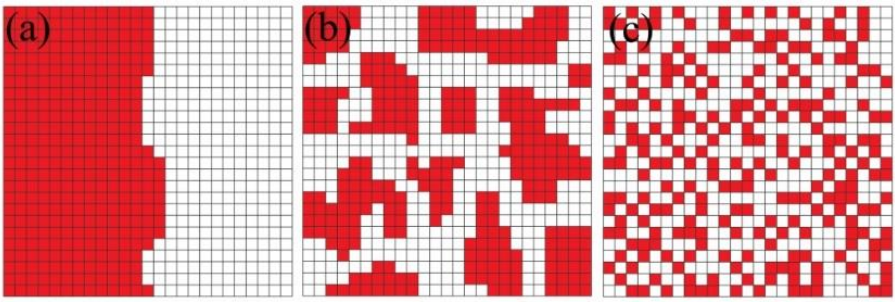

Figure 3.8 Illustration of disordered domains. (a) twinning; (b) the present structure; (c) disorder.

Conclusions

A new route of solving structures of twined crystals was introduced. An average structure in the space group $P4_2/n$ was obtained by using direct methods. Based on this average structure, 8 possible absolute structures were constructed and compared. The structure in the space group *Aea*2 was identified as the correct one by checking reflection conditions.

The disorder and twinning were refined simultaneously to achieve a good figures of merit. This does not necessarily mean that the two phenomenon occur at the same time but it implies that the domain size is in between the domain size for twinning and disorder.

4 Structure characterization from powder XRD

In the previous chapter we have mentioned that SXRD can provide very detailed structure information of a crystal, but it requires crystals with adequate size. In contrast, PXRD can be applied to crystals in much smaller size. This is crucial in many cases when big crystals are difficult to be synthesized. Moreover, PXRD provides the bulk information of the sample instead of the information from only a single crystal.
In this chapter, we will present four examples of structure determination of framework materials by using PXRD.

4.1 Complicated structure of GeO-JU90 germanate determined by PXRD (paper III)

As discussed in Chapter 1, open-framework germanates can be constructed by various GeO_x (x=4, 5, 6) polyhedra, which enable them to form structures more diverse than zeolites.
Jihong Yu's group at Jilin University synthesized the germanate GeO-JU90 by hydrothermal reactions using 1,5-bis(N-methylpyrrolidinium)pentane hydroxide as SDA. Extended X-ray absorption fine structure (EXAFS) technique was employed to analyze the local structure information. The average coordination number of Ge in GeO-JU90 is found to be 4.2, which is quite close to that of structures containing only GeO_4 tetrahedra. Thus it is quite interesting to reveal the crystal structure of this material.
The GeO-JU90 crystals are too thin for SXRD and are not stable enough for TEM analysis. The alternative way to reveal the structure is by PXRD.

Structure Solution

High resolution PXRD data was collected at Beamline I11, Diamond synchrotron light source. There are two major reasons to use synchrotron light source. First of all, the advanced detector and high

energy coherence of the X-rays give rise to much higher resolution compared to in-house diffractometers. High angular resolution can significantly reduce peak overlapping which is critical in structure determination by PXRD data. Secondly, the intense X-ray beam gives better statistics especially in the high angle range.

The charge flipping algorithm embedded in the program "superflip" was applied to solve the structure after extraction of peak intensity. The resultant electron density maps were assessed by the program to identify possible space groups. Then the program imposed the space group symmetries to the map to improve the signal to noise ratio. Ten electron density maps with the best figure of merit were saved. 6 out of 10 maps are in the space group *Amam* while the rest 4 maps are in the space group *Ama*2.

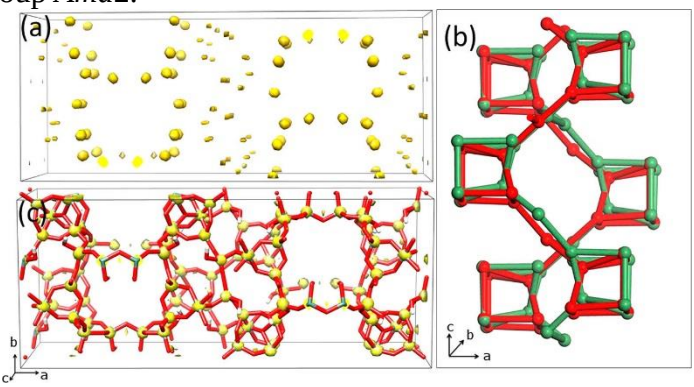

Figure 4.1 (a) electron density map in the space group Cmcm; (b) the overlapping Ge_7 clusters; (c) structure solution in the space group Cmc2.

Figure 4.1 (a) shows the electron density map in the space group *Amam*. It is obvious that the electron density aggregates to become discrete spots. However the spots in the middle part have significantly lower densities than those of the others. If we build the structure by assigning atoms to these spots, there will be overlapping of Ge_7 clusters in the middle part as shown in Figure 4.1(b). This overlapping is caused by the mirror symmetry which is included in *Amam* but not in *Ama*2. The structure built based on map in the space group *Ama*2, as shown in Figure 4.1(c) is free of overlapping and more reasonable from the chemical sense point of view. Thus the structure in *Ama*2 should be the correct one. The structure is quite complicated with 11 germanium atoms and 27 oxygen atoms in an asymmetric unit.

In the structure model, 56 out of the 88 germanium atoms in the unit cell obey the higher symmetry (*Amam*). This is probable the reason causing the ambiguous answer from the program "Superflip".

Structure refinement and allocating of guest molecules

After the structure model was built from the electron density map, Reitveld refinement was applied to the structure model. Soft restrains on the bond lengths and bond angles were imposed to keep the structure intact during the refinement. Different "ideal" bond lengths and angles were set for Ge atoms in different coordination environment (1.74 Å for GeO_4 tetrahedra, 1.76Å and 1.95 Å for GeO_5 bipyramid, 1.88 for GeO_6 octahedra, and the bond angles were set according to the geometry of the polyhedra).

After the refinement on the framework, it was found that the calculated peaks in the low 2θ angle ranges have significant higher intensity compared to the observed peaks. It is most probably due to the absence of guest molecules in the structure model. Except for the guest molecules, there are also some other factors that could affect the intensities of the peaks in a certain 2θ range. For instance, the scale factor applies to the intensity of all peaks, absorption factor mainly affects the peaks at high 2θ angle and atomic displacement parameters mainly affect the peaks at high 2θ angles. Hence during the refinement, a good understanding of the effects of each parameter on diffraction pattern is necessary to interpret the data correctly.

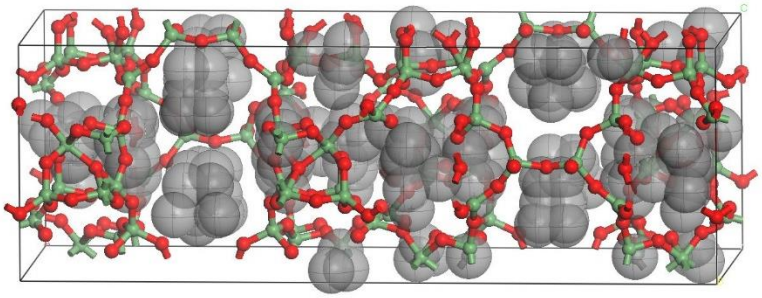

Figure 4.2 Random carbon atoms aggregate into groups after simulated annealing.

The guest molecules were located by using the simulated annealing method. Instead of using the whole molecule as a rigid body, we added 10 carbon atoms at random positions. After the simulated annealing, the carbon atoms aggregated into groups as illustrated in Figure 4.2. The one located in the channel along *a*-axis is in the shape similar to the SDA molecule. The other two in the channels perpendicular to the *a*-axis are significantly smaller than the SDA molecules, which implies possible decomposition of the SDA molecules. Alternatively, it is also possible that the SDAs remained intact but the pentane group connecting the two N-methylpyrrolidine groups were too weak to been

seem due to the low electron density.

Through liquid state ^{13}C MAS NMR spectrum on a digested sample, it was found that the SDA molecules were kept intact after the synthesis. Hence two SDA molecules were added into the structure as rigid body. Their position and conformation were refined against the powder pattern. The SDA in the channel along *a*-axis is in almost linear conformation while the other one is slightly bent. There were a residual peaks found from the Fourier difference map. It could be water molecule or small cation e.g. NH_4^+. By considering the charge balance, the peak was then assigned as NH_4^+.

After adding the guest molecules, a satisfactory fit of the experimental and calculated pattern was reached. The resultant agreement factors are R_p = 6.650%, R_{wp} = 9.678%, R_{exp} = 1.859% and R_{bragg} = 4.781%.

Structure description

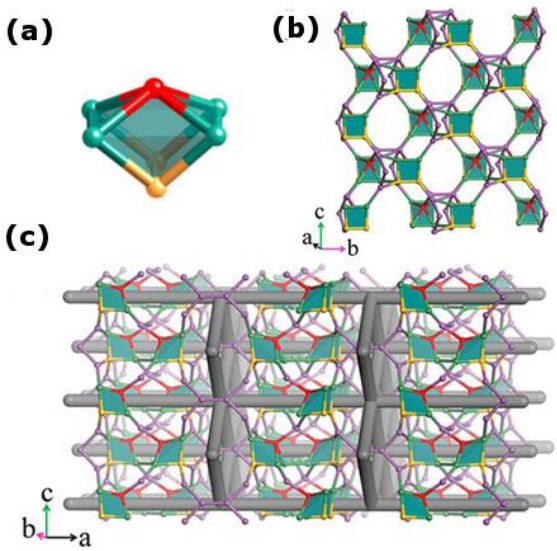

Figure 4.3 (a) GeO_5 bipyramid; (b) the layered building unit; (c) the structure of GeO-JU90. The grey pillars refer to the channel system.

GeO-JU90 crystallizes in an orthorhombic unit cell in the space group *Ama*2 with lattice parameters of *a* = 37.8296 (4), *b* = 15.2437 (2) and *c* = 12.8365 (1). The framework structure is composed of Ge_7 clusters and the bridging GeO_4 / $GeO_3(OH)$ tetrahedra. The layered building units possess 11-ring channels along the direction

perpendicular to the layer. The layers are connected through the $GeO_3(OH)$ tetrahedra to form a 3D framework with 11 × 12 × 12-ring channels.

Conclusions

The structure of a complicated open framework germanate was solved from PXRD data by the charge-flipping algorithm. In the asymmetric unit of the framework structure, there are 11 Ge atoms and 27 O atoms, implying the highly complexity of the structure. The structure constructed from Ge_7 clusters and additional $GeO_3(OH)$ units possesses an interesting 12 × 12 × 11-ring channel system. The guest molecules in the channels are located by using simulated annealing method, which were also confirmed by NMR analysis.

4.2 Structure of Zn-ptcda MOF determined by PXRD (paper IV)

A nano-sized crystalline MOF was synthesized and used as a precursor for the synthesis of metal-oxide nanoparticles with desired morphology. The MOF was made of $Zn(OAc)_2$ and perylene-3, 4, 9, 10-tetracarboxylic dianhydride (ptcda) ligand. Although small crystal sizes are desirable to produce nano metal oxide particles, they also introduce difficulties in the structure determination of the as-made MOF crystals. Here we solved the structure by PXRD.

Structure solution and structure refinement

The PXRD pattern was indexed by an orthorhombic lattice with parameters of a = 9.7441 (8) Å, b = 7.0209 (7) Å, c = 14.268 (1) Å. Then the reflection conditions (0kl: k = 2n, h0l: h = 2n, h00: h = 2n and 0k0: k = 2n) were deduced from the PXRD pattern. According to these reflection conditions, the space group was determined to be either *Pba*2 or *Pbam*. The high symmetry one Pbam was tested firstly. The intensity of each reflection was extracted to give a list of 523 reflections. The structure was solved using these reflections by direct methods using the program "SHELX97". The zinc and oxygen atoms were found. The rest of carbon atoms were located by considering the conformation of the ligand molecules, bond distances and the difference Fourier map.

The structure solution was then refined against the PXRD pattern by

the Rietveld method. The final structure is in a good agreement with the PXRD pattern, as shown in Figure 4.4. The R factors converged to R_p = 4.76%, R_{wp} = 6.53%, R_b = 2.25%.

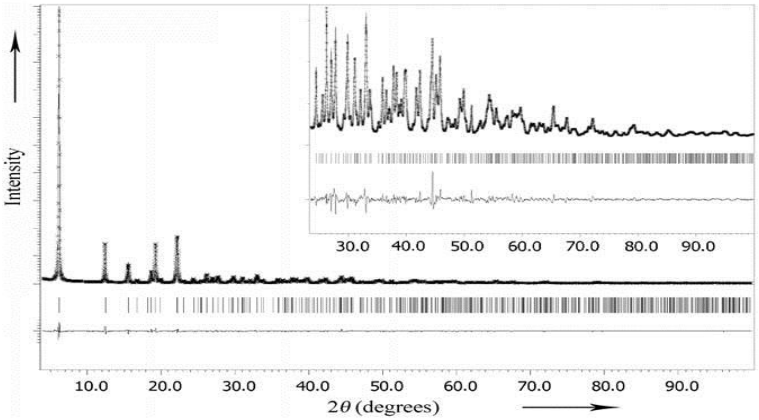

Figure 4.4 The Rietvelt refinement result including the plot of the experimental pattern, the calculated pattern, the difference curve and peak positions (wavelength: 1.5406 Å).

Structure description

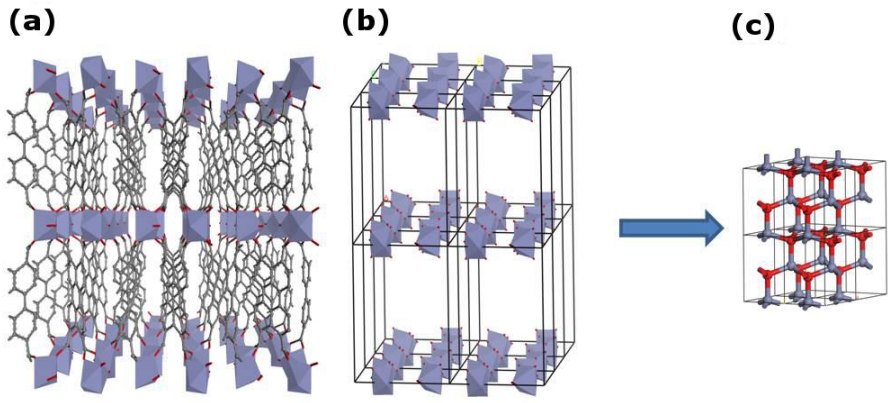

Figure 4.5 (a) The structure of Zn-ptcda; (b) the structure with only chains of zinc oxide octahedra; (c) the zinc oxide structure.

Each zinc atom is coordinated to 4 carboxylate groups and 2 water molecules to form an octahedron. The octahedra are connected by the ptcda ligands to form chains which are interlinked by the ligands to build up the 3D framework as shown in Figure 4.5. When heated at 370^{o}C, the structure collapsed and formed zinc oxide nanoparticles with morphology inherited.

4.3 Germanate SU-77 determined by combining TEM and PXRD (paper V)

In the previous sections of this chapter, structures are solved and refined by PXRD. However, solving structures from PXRD requires the sample to be pure and in some difficult cases it requires expertise and considerable time. RED resembles the process of SXRD. After data collection and reduction, the programs for SXRD structure solution can be employed for RED data. In this project, RED and PXRD were combined in the structure determination.

Germanate SU-77 was synthesized under hydrothermal condition using ethylenediamine as the SDA by Liang Fang in Dr. Feifei Gao's group at Stockholm University.

Structure solution and refinement

The RED data of crystal SU-77 containing 396 electron diffraction patterns was recorded and processed to reconstruct the 3D reciprocal lattice. The obtained unit cell parameters are a = 14.19 Å, b = 12.66 Å, c = 9.52 Å, α = 89.89°, β = 89.91°, γ = 89.60°. Since the angles are close to 90 °, the crystal was expected to be in orthorhombic. From the reflection conditions and the intensity distribution, the space group *Pnam* was deduced. The structure was then solved by using the program "SHELXS97".

High resolution PXRD data of SU-77 collected at the synchrotron light source was used for structure refinement. Indexing the PXRD pattern resulted in a monoclinic unit cell of a = 13.52427(5) Å, b = 12.64862(5) Å, c = 9.60578(3) Å, β = 92.8599(4) ° which deviated slightly from that obtained from the RED data. The difference between the results from RED and PXRD are most probably caused by a structure transformation triggered by the electron beam. Since X-rays interact with matter weakly, the as-made structure is always preserved during PXRD data collection. While for the RED method, due to the strong interaction between electrons and matter, the structure transformation may be trigged. Thus it is supposed that the as-make crystals are in the monoclinic unit cell but transform to the orthorhombic one under the electron beam.

To solve the structure of the as-made crystals, the monoclinic unit cell from PXRD was combined with reflection indices and intensities from RED. The space group $P2_1/a$ was deduced from the reflection conditions. A structure model was obtained by using the program

"SHELXS97".

Reitveld refinement of framework structure against the PXRD pattern was carried out with soft restrains on the Ge-O bond lengths and the O-Ge-O bond angles. Although the refinement gave out a high R_{wp} value of 0.219. From the difference Fourier map, some hints of the location of SDA molecules were found (Figure 4.6). Firstly, in the channel along [001] direction, two groups of peaks was found. Assigning C and N atoms to these peaks resulted in two independent ethylenediamine molecules. Secondly, it was found that two strong peaks appearing next to the terminal O atoms of the Ge octahedron. The distance between the peaks and O atoms are around 1.5Å, which is too long for hydrogen bond but similar to the length of C-N bond. Therefore the O atoms were replaced by N atoms and the peaks were assigned as C atoms, which gave out an ethylenediamine molecule coordinating to the Ge atom.

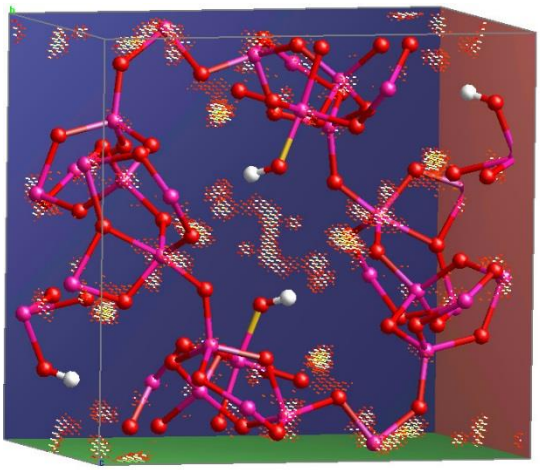

Figure 4.6 Difference Fourier map from the refinement of the framework structure against PXRD

From the fluorine analysis, it was found that there was 3.2 wt% of fluorine in the sample. It indicates that the OH^- group should be F^-. This makes the octahedral Ge atom coordinates to two N atoms from the same SDA molecule, one F atom and three bridging O atoms.

The new model was built by implementing the changes mention above and the final Rietveld refinement result in Figure 4.7 shows a good fit between the experimental and calculated patterns (R_p = 0.0663, R_{wp} = 0.0834, R_{exp}= 0.0371, GOF = 2.25, R_{bragg} = 0.0299).

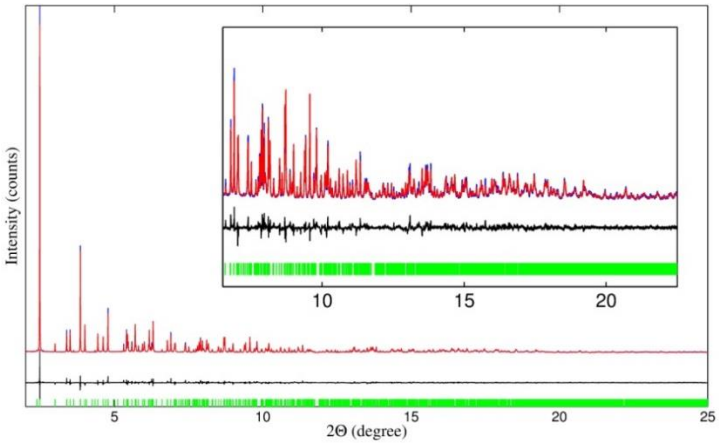

Figure 4.7 Result of the Rietveld refinement. Blue: experimental pattern; red: calculated pattern; black: difference; green: reflection peak position (wavelength: 0.8271 Å).

The thermogravimetric analysis (TGA) shows 15% of weight loss from 200 ºC to 600 ºC, which suggests eight SDA molecules per unit cell. This result is consistent with the refinement result. Among this eight molecule, the four coordinating to Ge atom should be neutral and the rest four can be eight neutral or protonated. According to the present model, the framework carries four negative charge which suggests the four SDAs in the channel carries one positive charge each. Hence the formula of SU-77 was deduced to be $|(C_2H_9N_2)_4(C_2H_8N_2)_4|[Ge_{24}O_{48}F_4]$. This formula fits the CHN analysis well but shows different F content as in the fluorine analysis result which suggest one more F per unit cell. This extra F content could be from the F^- anion residing in the channels or cages. However due to the small quantity, it is difficult to locate them from X-ray diffraction. In this case, SDAs should be considered to carry more positive charges to balance both the framework charge and F^- anions. Hence the formula is finally determined to be $|(C_2H_{10}N_2)(C_2H_9N_2)_3(C_2H_8N_2)_4F|[Ge_{24}O_{48}F_4]$.

Structure description

The basic building unit of the SU-77 framework is the Ge_6 cluster $Ge_6O_{17}(C_2H_8N_2)$ F shown in Figure 4.8(a) which consists of three GeO_4 tetrahedra, two GeO_5 bipyramid and one $GeO_3(C_2H_8N_2)F$ octahedra. The Ge_6 cluster is similar to the Ge_7 cluster (Figure 4.8(b)) which is a more commonly appearing building unit. The Ge_6 clusters are connected to form chains (Figure 4.8(c)) and the chains are linked by

sharing oxygen atoms to build up the 3D framework (Figure 4.8(e)).

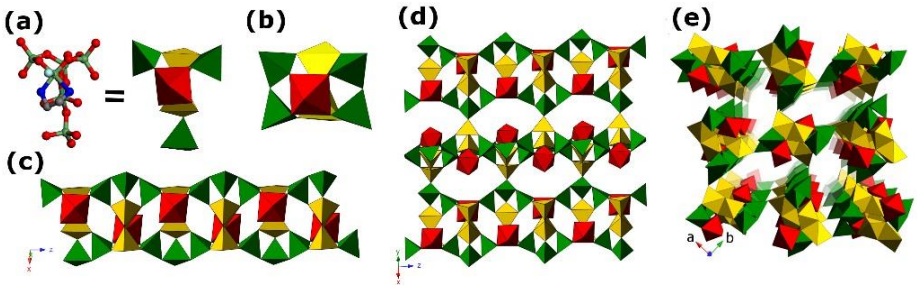

Figure 4.8 (a) Ge_6 cluster; (b) Ge_7 cluster, (c) chain building unit; (c) a layer reviewed along the [110] direction, and (d) framework structure of SU-77.

Structure transformation

The Structure transformation of SU-77 can be trigged not only by electron beam but also by heating. In-situ PXRD patterns at different temperatures revealed the structure transformation occurred at around 200 ºC. The pattern of high temperature phase can be indexed by an orthorhombic unit cell with parameters of a=13.454 Å, b=12.652 Å and c=9.619 Å.

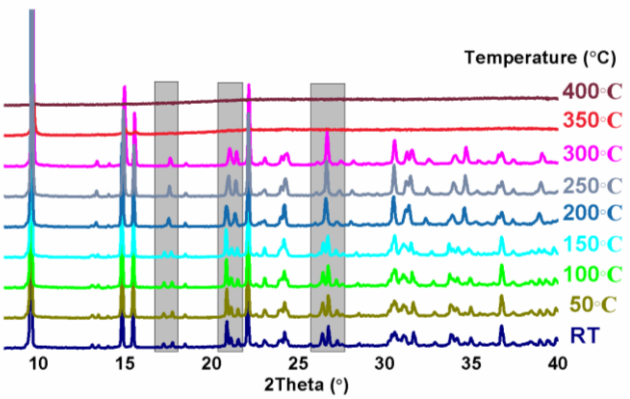

Figure 4.9 In-situ PXRD patterns at different temperature.

Conclusions

The structure of as-made SU-77 was determined by combining 3D electron diffraction data and PXRD data. The number and species of guest molecules in the channels were determined by combining information from elemental analysis, TGA and charge balance principle. The framework with a 12× 10 × 10-ring channel system can be described as the relative dense chains of new Ge_6 clusters linked

through sharing oxygen atoms to form the 3D framework. It was found that a structure change of SU-77 from monoclinic to orthorhombic can be trigged by both exposing to electron beam and heating.

4.4 Characterization of structure transformation of NOTT-202 MOF by in-situ PXRD (paper VI)

MOFs are studied extensively because of their excellent properties and great application potential in gas adsorption and storage. For instance HKUST-1 shows a higher volumetric methane up-take (267 cc(STP)/cc at 65 bar) than the target set by the US Department of Energy[52].
NOTT-202 is a MOF material synthesized by Dr. Sihai Yang from the University of Nottingham. NOTT-202 represents the as-made form of the material with a partially interpenetrated framework. After desolvation, the framework changed to a fully occupied double interpenetrated framework named NOTT-202a. It was found that NOTT-202a is an excellent CO_2 adsorbent with both high uptake and selectivity.

SO_2 is another species that causes serious environmental problems. However, due to the high corrosive nature of SO_2, framework materials are rarely stable when exposed to SO_2. NOTT-202a shows an excellent SO_2 uptake property of 13.6 mmol/g at 268 K and 1.0 bar which is the highest value among all framework materials.

In order to better understand the adsorption mechanism, high resolution in-situ PXRD patterns were collected during the SO_2 adsorption and desorption process. As shown in Figure 4.10, a strong reflection peak appeared when the SO_2 pressure increased to 540 mbar, which indicates a phase transformation during the adsorption process. After the desorption process, the peaks from NOTT-202a disappeared but the peaks from the new phase were preserved.

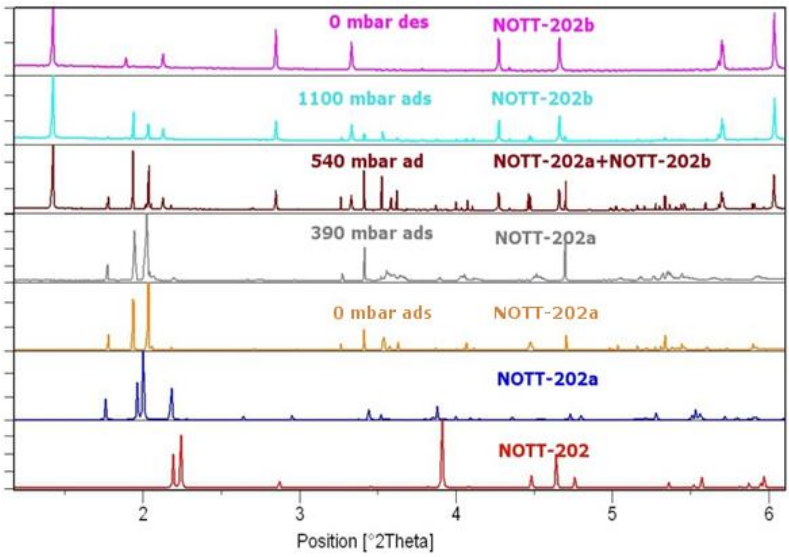

Figure 4.10 Simulated PXRD patterns of NOTT-202, NOT-202a at the ambient conditions and in-situ PXRD patterns of NOTT-202a during SO_2 adsorption and desorption process.

NOTT-202a

The pattern at 0 mbar adsorption is different from that simulated from the NOTT-202a structure determined from SXRD data at ambient conditions. As a quite flexible structure, some structural changes e.g. shrinking or expanding, may occur when vacuuming the sample. We indexed and solved the structure from the in-situ PXRD pattern (0 mbar ads).

Table 4.1 Unit cell parameters of the NOTT-202a structure at the ambient and vacuum conditions.

	a (Å)	*b* (Å)	*c* (Å)	α (°)	β (°)	γ (°)
Ambient condition	19.523(7)	28.812(10)	27.015(10)	90.00	94.929(6)	90.00
0 mbar ads	19.0510(7)	29.3430(9)	28.095(1)	90.00	89.079(1)	90.00

By indexing the patterns, it was found that the β angle changed by almost 5° after vacuuming. The structure was then solved from a real space method - simulated annealing. Two structure fragments including indium atoms and the carboxylate ligand molecule were used. The bipyenyl-3, 3', 5, 5'-tetra-(phenyl-4-carboxylate) (L^{4-}) was set as a rigid body with 15 refinable parameters including 9 for torsion angles (shown in Figure 4.11), 3 for rotation angles and 3 for positions. In each cycle of the simulated annealing process, the structure fragments were first

given random positions and then all the parameters were refined to minimize the figure of merit. In order to simulate the annealing process, the damping factor was relatively big in the beginning of each cycle and kept decreasing as it proceeded. After 600 cycles, the structure model with the best figure of merit was picked out (Figure 4.11(b)). The structure is similar to that solved from SXRD. It has a 2-fold interpenetrated framework in which the indium atoms are 7-coordinated and connected to 4 carboxylate groups.

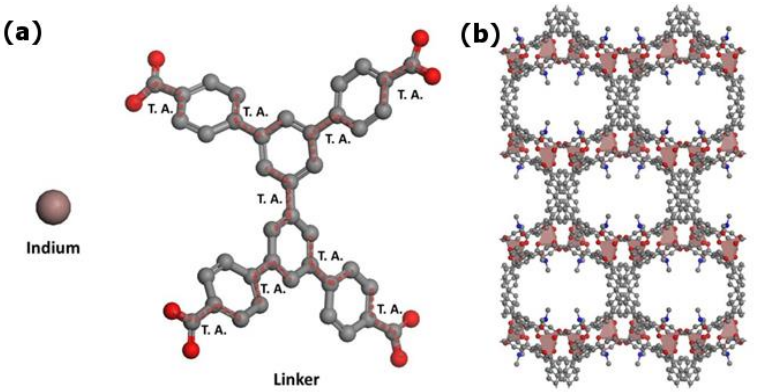

Figure 4.11 (a) Two structure fragments in NOTT-202a. (b) structure obtained from simulated annealing.

NOTT-202b

Table 4.2 The unit cell parameters of NOTT-202a and NOTT-202b

	a (Å)	*b* (Å)	*c* (Å)	*α* (°)	*β* (°)	*γ* (°)
NOTT-202	16.512(7)	25.952(11)	30.569(12)	90.00	90.00	90.00
NOTT-202b	7.558(2)	26.652(2)	30.013(5)	90.00	89.01(3)	90.00

The structure determination of NOTT-202b was far more problematic than that of NOTT-202a, because the PXRD pattern of NOTT-202b has only a handful of peaks. The pattern of NOTT-202b was indexed using a monoclinic unit cell with parameters shown in Table 4.2. It was found that the unit cell of NOTT-202b is quite similar to that of NOTT-202, the structure of the as-synthesized material before desolvation. The only conspicuous difference is the unit cell parameter *a*. It is believed that the nets are in similar conformation in these two materials but there are shift and rotation between the interpenetrated nets. Thus the structure model of NOTT-202b was built based on the net in NOTT-202.

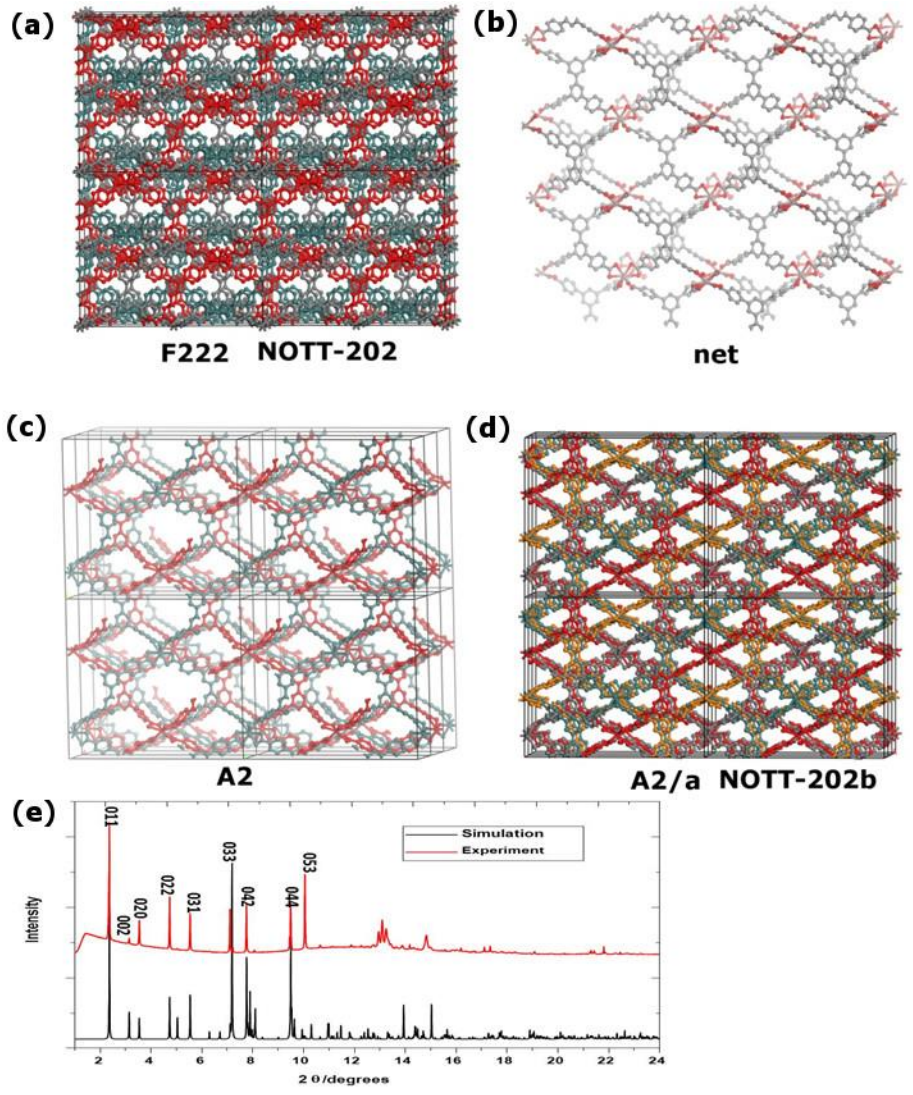

Figure 4.12 (a) Structure of NOTT-202; (b) A single net in NOTT-202; (c) The model in space group A2; (d) The model in space group A2/a; (e) Simulated PXRD pattern of the built model and experimental PXRD pattern of NOTT-202b.

There are three nets in the NOTT-202a structure. If two of them are deleted and only one net is left in the structure, the symmetry decreases from *F*222 to *A*2. This implies that *A*2 is the symmetry embedded in the net. Fitting this net into the unit cell of NOTT-202b induces slight distortions of the net and the halved unit cell generated a copy of the net which shifts one unit cell from the original one along the *a*-axis (as shown in Figure 4.12 (c)). The space group of the model at this stage is *A*2, the same as the one embedded in the net. But by analyzing the

reflection condition, it was found that only reflections of *hkl:k+l*=2*n* and *h*00:*h*=2*n* appeared in the PXRD pattern, which indicated an A-centering and an *a*-glide perpendicular to *b*-axis in the structure. Thus the a-glide was added to the structure which consequently generated the other two nets. This structure model of NOTT-202b is similar to the NOTT-202 structure except that the second net of NOTT-202 shifts by *c*/4 - *b*/6. In addition, the *a*-axis is halved which created two equally occupied positions for each net, resulting the highly disordered structure upon SO_2 adsorption. The simulated pattern is similar to the experimental one but they are still some disagreements. A reasons is that the disorder along the *a*-axis decreases the periodicity along that direction and thus causes the absence of the reflections hkl with h = 0.

Conclusions

The NOTT-202a material with excellent SO_2 uptake was analyzed by using in-situ PXRD. A dramatic phase transformation was detected during the SO_2 adsorption and desorption process. The partially interpenetrated NOTT-202 framework changed to NOTT-202b after desolvation and then changed to highly disordered structure of NOTT-202b with similar net conformation as NOTT-202.

5 Conclusions and future work

The thesis includes the synthesis of zeolite ITQ-33 single crystals, investigation of disordered structures and structure solution and refinement from PXRD data. The main conclusions of this thesis include:

1. We synthesized single crystals of zeolite ITQ-33 and collected the SXRD data. It was found that due to the special structure feature, the bridging D4R units have two choices of positions with equal possibilities. This introduces sever disordering in the structure. It was also found that there are 10-ring pores inside the ordered domains and they become to 11-ring pores at the boundary.
2. Two disordered structures (zeolite ITQ-33 crystal and a metal organic complex [2Fe3S] crystal) were refined by SXRD, it was found that domain sizes shall be taken into consideration.
3. A new method was proposed for solving structure of merohedric or pseudo-merohedric twinning crystals from real space average structures.
4. Structures of open-framework germanates GeO-JU90 and SU-77 were solved by PXRD solely and combining RED and PXRD, respectively. The features of the structures as well as structure transformation were investigated. Simulated annealing combined with other chemical analysis methods were used to allocate the guest molecules in the channels.
5. The structures of two MOF materials were investigated by PXRD. The structure of a Zn-ptcda MOF is solved by using direct methods and refined by using Rietveld method. For the NOTT-202 MOF, a structure transformation during the SO_2 adsorption and desorption process was observed and investigated by in-situ PXRD. The phase of NOTT-202a was detected before adsorption at 0 mbar and it transformed to NOTT-202b during the increase of SO_2 up-take. A structure model was built based on the as-made NOTT-202 structure.

There is still much work that I wish to carry out but I haven't done yet due to the limited time of PhD study.

1. The disordering in ITQ-33 material is quite unique. It changes the pore size of the structure from 10-ring to 11-ring. If we could facilitate the occurring of the disorder, it would give rise to a structure different from the average one and the new material would show different catalytic and adsorption properties.
2. We have used both PXRD and RED to solve structures of nano-sized crystals. PXRD provide data with high accuracy and high completeness. RED provides 3D data. In some difficult cases, it is difficult to solve the structure from any of the two methods alone e.g. in the cases of the poor crystalline materials and beam sensitive crystals. It would be very interesting to develop an algorithm takeing data from both of the methods into account. For example, it can use the intensity of the reflections from the RED data as a clue for the repartitioning of the overlapping reflections in the PXRD data.

6 Acknowledgements

Firstly, I would like to thank my supervisor Junliang Sun who guided me during these 4 years. I knew almost nothing about porous materials and crystallography before I came to Stockholm. Thank you for guiding me into this wonderful world. Besides, your broad knowledge and the way of thinking inspired me a lot. I also enjoyed the discussions with you about the topics outside the PhD project.

Secondly, I want to thank my co-supervisor Xiaodong Zou. Your rigorous scholarship sets an example for me. You guidance and advices are important to me. I truly appreciate you sharing your experience and opinions with me.

I thank Sven Hovmöller for your corrections on my written and spoken English. Thank you for your great passion as well as patience. I want to thank Wei Wan for your corrections on my thesis. You did it faster and more carefully than any super computer can do. I also want to thank Feifei Gao for your advices and suggestions. Thanks to Mats Johnsson and Osamu Terasaki, Zhijian Shen, Niklas Hedin and Gunnar Svensson, for your help and friendly conversation.

Thanks to the collaborators, Yan Xu, Jihong Yu, Liang Fang, Feifei Gao, Mingrun Li, Sihai Yang. You have provided excellent samples.

Thanks to Kjell Jansson, Tom Willhammar, Cheuk-Wai Tai, Lars Eriksson, Zoltán Bascik for your training on various equipments.

Thanks to the administrative staff, Ann-Britt Rönnell, Hanna Nyholm, Anna-Karin Olsson, Pia Raninen and Daniel Emanuelsson. Your work makes the life much easier for a foreign student.

I am also very grateful to the help from my colleagues Zhengbao Yu, A. Ken Inge, Jie Su, Yifeng Yun, Hong Chen, Tom Willhammar, Haoquan Zheng, Peng Guo, Fabian Carson, Ana Platero Yi Zhang, Amber Mace and Shiliang Huang. The discussions with you and helps from you are much appreciated.

Thanks to other colleagues in the group, since the life without you

would be so boring. You are Mikaela Gustafsson, Yunxiang Li, Xin Xia, Elina Kapaca, Alexandra Neagu, Hani Abdelhamid, Jie Liang, Liang Fang, Fei Peng, Yunchen Wang, Qingpeng Meng, Changjiu Xia, Junzhong Lin, Ning Yuan, Justin Xu, Saskia Vanpeene and Dung Trung Tran,

Thanks to the colleagues in MMK, Jianfeng Hu, Yonglei Wang, Ji Zou, Ocean Cheung, Daniel Eklöf, Guang Han, Wenming Hao, Shichao Hu, Gholamhasan Teymoori, Sumit Konar, Duan Li, Yanhang Ma, Neda Keshavarzi, Ojwang Dickson, Bin Qian, Yang Shen, Chao Xu, Daqing Cui, Christina Schütz, and Yuan Zhong. You make the department home to me.

Thanks to the football mates, German Salazar-Alvarez, Farid Akhtar, Zoltán Bacsik, Alfonso Garcia-Bennett, Jianfeng Hu, Ibarra Illich, Julien Navarro, Haoquan Zheng, Fabian Carson, Wenming Hao, Yunliang Liu, Yanghan Ma, Dickson Ojwang, Chao Xu, Arnaud Mayence, Changjiu Xia and Ge Yin. I enjoyed all of the football games with you.

Finally I want to thank all my friends and family members for your support. You are my most precious wealth.

7 Reference

1. Bellussi, G., Carati, A., Rizzo, C. & Millini, R. New trends in the synthesis of crystalline microporous materials. *Catal. Sci. Technol.* **3,** 833 (2013).
2. Qiang Xu. *Nanoporous Materials:Synthesis and Applications*. (2013). at <http://www.crcpress.com/product/isbn/9781439892053>
3. Kuznicki, S. M. *et al.* A titanosilicate molecular sieve with adjustable pores for size-selective adsorption of molecules. *Nature* **412,** 720–724 (2001).
4. Cheetham, A. K., Férey, G. & Loiseau, T. Open-Framework Inorganic Materials. *Angew. Chem. Int. Ed.* **38,** 3268–3292 (1999).
5. Yaghi, O. M. *et al.* Reticular synthesis and the design of new materials. *Nature* **423,** 705–714 (2003).
6. Schüth, F. & Schmidt, W. Microporous and Mesoporous Materials. *Adv. Mater.* **14,** 629–638 (2002).
7. Kresge, C. T., Leonowicz, M. E., Roth, W. J., Vartuli, J. C. & Beck, J. S. Ordered mesoporous molecular sieves synthesized by a liquid-crystal template mechanism. *Nature* **359,** 710–712 (1992).
8. Jiang, J. *et al.* Synthesis and Structure Determination of the Hierarchical Meso-Microporous Zeolite ITQ-43. *Science* **333,** 1131–1134 (2011).
9. Lin, H.-Y. *et al.* Crystalline Inorganic Frameworks with 56-Ring, 64-Ring, and 72-Ring Channels. *Science* **339,** 811–813 (2013).
10. Deng, H. *et al.* Large-Pore Apertures in a Series of Metal-Organic Frameworks. *Science* **336,** 1018–1023 (2012).
11. Zones, S. I. Translating new materials discoveries in zeolite research to commercial manufacture. *Microporous Mesoporous Mater.* **144,** 1–8 (2011).
12. Kitagawa, S., Kitaura, R. & Noro, S. Functional Porous Coordination Polymers. *Angew. Chem. Int. Ed.* **43,** 2334–2375 (2004).

13. McCusker, L. B. & Baerlocher, C. in *Stud. Surf. Sci. Catal.* (Jiří Čejka, H. van B., Avelino Corma and Ferdi Schüth) **Volume 168,** 13–37 (Elsevier, 2007).
14. Davis, M. E. & Lobo, R. F. Zeolite and molecular sieve synthesis. *Chem. Mater.* **4,** 756–768 (1992).
15. Flanigen, E. M. in *Stud. Surf. Sci. Catal.* (H. van Bekkum, E. M. F., P. A. Jacobs and J. C. Jansen) **Volume 137,** 11–35 (Elsevier, 2001).
16. Cundy, C. S. & Cox, P. A. The Hydrothermal Synthesis of Zeolites: History and Development from the Earliest Days to the Present Time. *Chem. Rev.* **103,** 663–702 (2003).
17. Robert M. Milton. in *Zeolite Synth.* **398,** 1–10 (American Chemical Society, 1989).
18. Barrer, R. M. & Denny, P. J. 201. Hydrothermal chemistry of the silicates. Part IX. Nitrogenous aluminosilicates. *J. Chem. Soc. Resumed* 971–982 (1961). doi:10.1039/JR9610000971
19. Ch., Baerlocher & L.B., McCusker. Database of Zeolite Structures: http://www.iza-structure.org/databases/.
20. Gibbs, G. V., Boisen, M. B., Hill, F. C., Tamada, O. & Downs, R. T. SiO and GeO bonded interactions as inferred from the bond critical point properties of electron density distributions. *Phys. Chem. Miner.* **25,** 574–584 (1998).
21. Jiang, J. *et al.* Investigation of Extra-Large Pore Zeolite Synthesis by a High-Throughput Approach. *Chem. Mater.* **23,** 4709–4715 (2011).
22. Breck, D. W. Crystalline molecular sieves. *J. Chem. Educ.* **41,** 678 (1964).
23. Kerr, G. T. Chemistry of Crystalline Aluminosilicates. I. Factors Affecting the Formation of Zeolite A. *J. Phys. Chem.* **70,** 1047–1050 (1966).
24. De Moor, P.-P. E. A. *et al.* Imaging the Assembly Process of the Organic-Mediated Synthesis of a Zeolite. *Chem. – Eur. J.* **5,** 2083–2088 (1999).
25. Sherman, J. D. Synthetic zeolites and other microporous oxide molecular sieves. *Proc. Natl. Acad. Sci.* **96,** 3471–3478 (1999).
26. Akhtar, F., Liu, Q., Hedin, N. & Bergström, L. Strong and binder free structured zeolite sorbents with very high CO2-over-N2 selectivities and high capacities to adsorb CO2 rapidly. *Energy Environ. Sci.* **5,** 7664–7673 (2012).
27. Liu, Q. *et al.* NaKA sorbents with high CO2-over-N2 selectivity and high capacity to adsorb CO2. *Chem. Commun.* **46,** 4502–4504 (2010).

28. Martínez, C., Verboekend, D., Pérez-Ramírez, J. & Corma, A. Stabilized hierarchical USY zeolite catalysts for simultaneous increase in diesel and LPG olefinicity during catalytic cracking. *Catal. Sci. Technol.* **3,** 972–981 (2013).
29. Zečević, J., Gommes, C. J., Friedrich, H., de Jongh, P. E. & de Jong, K. P. Mesoporosity of Zeolite Y: Quantitative Three-Dimensional Study by Image Analysis of Electron Tomograms. *Angew. Chem. Int. Ed.* **51,** 4213–4217 (2012).
30. Chen, N. Y. in *Stud. Surf. Sci. Catal.* (J.W. Ward) **Volume 38,** 153–163 (Elsevier, 1988).
31. Schipper P. H., Dwyer F. G., Sparrell P. T., Mizrahi S. & Herbst J. A. in *Fluid Catal. Crack.* **375,** 64–86 (American Chemical Society, 1988).
32. Olsbye, U. *et al.* Conversion of Methanol to Hydrocarbons: How Zeolite Cavity and Pore Size Controls Product Selectivity. *Angew. Chem. Int. Ed.* **51,** 5810–5831 (2012).
33. Dai, W., Wu, G., Li, L., Guan, N. & Hunger, M. Mechanisms of the Deactivation of SAPO-34 Materials with Different Crystal Sizes Applied as MTO Catalysts. *ACS Catal.* **3,** 588–596 (2013).
34. White, J. L. Methanol-to-hydrocarbon chemistry: The carbon pool (r)evolution. *Catal. Sci. Technol.* **1,** 1630–1635 (2011).
35. Yu, J. & Xu, R. Rational Approaches toward the Design and Synthesis of Zeolitic Inorganic Open-Framework Materials. *Acc. Chem. Res.* **43,** 1195–1204 (2010).
36. Huang, S. Open-Framework Germanates and Nickel Germanates : Synthesis and Characterization. (2012). at <http://www.diva-portal.org/smash/record.jsf?pid=diva2%3A516900>
37. Inge, A. K. Open-Framework Germanates : Synthesis, Structure, and Characterization. (2012). at <http://www.diva-portal.org/smash/record.jsf?searchId=1&pid=diva2:523727>
38. Martoňák, R., Donadio, D., Oganov, A. R. & Parrinello, M. From four- to six-coordinated silica: Transformation pathways from metadynamics. *Phys. Rev. B* **76,** 014120 (2007).
39. Li, H., Eddaoudi, M. & Yaghi, O. M. An Open-Framework Germanate with Polycubane-Like Topology. *Angew. Chem. Int. Ed.* **38,** 653–655 (1999).
40. Li, H., Eddaoudi, M., Richardson, D. A. & Yaghi, O. M. Porous Germanates: Synthesis, Structure, and Inclusion Properties of Ge7O14.5F2 {(CH3)2NH2]3(H2O)0.86. *J. Am. Chem. Soc.* **120,** 8567–8568 (1998).

41. Villaescusa, L. A., Lightfoot, P. & Morris, R. E. Synthesis and structure of fluoride-containing GeO2 analogues of zeolite double four-ring building units. *Chem. Commun.* 2220–2221 (2002). doi:10.1039/B207374A
42. Zou, X., Conradsson, T., Klingstedt, M., Dadachov, M. S. & O'Keeffe, M. A mesoporous germanium oxide with crystalline pore walls and its chiral derivative. *Nature* **437,** 716–719 (2005).
43. Christensen, K. E. Design of open-framework germanates. *Crystallogr. Rev.* **16,** 91–104 (2010).
44. Han, Y., Li, Y., Yu, J. & Xu, R. A Gallogermanate Zeolite Constructed Exclusively by Three-Ring Building Units. *Angew. Chem. Int. Ed.* **50,** 3003–3005 (2011).
45. Zhou, H.-C., Long, J. R. & Yaghi, O. M. Introduction to Metal–Organic Frameworks. *Chem. Rev.* **112,** 673–674 (2012).
46. Wang, C., Zhang, T. & Lin, W. Rational Synthesis of Noncentrosymmetric Metal–Organic Frameworks for Second-Order Nonlinear Optics. *Chem. Rev.* **112,** 1084–1104 (2012).
47. Stock, N. & Biswas, S. Synthesis of Metal-Organic Frameworks (MOFs): Routes to Various MOF Topologies, Morphologies, and Composites. *Chem. Rev.* **112,** 933–969 (2012).
48. Li, M., Li, D., O'Keeffe, M. & Yaghi, O. M. Topological Analysis of Metal–Organic Frameworks with Polytopic Linkers and/or Multiple Building Units and the Minimal Transitivity Principle. *Chem. Rev.* **114,** 1343–1370 (2014).
49. Borfecchia, E. *et al.* Insights into Adsorption of NH_3 on HKUST-1 Metal–Organic Framework: A Multitechnique Approach. *J. Phys. Chem. C* **116,** 19839–19850 (2012).
50. Mason, J. A., Veenstra, M. & Long, J. R. Evaluating metal–organic frameworks for natural gas storage. *Chem. Sci.* **5,** 32–51 (2013).
51. Wu, H. *et al.* Metal–Organic Frameworks with Exceptionally High Methane Uptake: Where and How is Methane Stored? *Chem. – Eur. J.* **16,** 5205–5214 (2010).
52. Peng, Y. *et al.* Methane Storage in Metal–Organic Frameworks: Current Records, Surprise Findings, and Challenges. *J. Am. Chem. Soc.* **135,** 11887–11894 (2013).
53. Cavka, J. H. *et al.* A New Zirconium Inorganic Building Brick Forming Metal Organic Frameworks with Exceptional Stability. *J. Am. Chem. Soc.* **130,** 13850–13851 (2008).
54. Wu, H. *et al.* Unusual and Highly Tunable Missing-Linker Defects in Zirconium Metal–Organic Framework UiO-66 and Their

Important Effects on Gas Adsorption. *J. Am. Chem. Soc.* **135,** 10525–10532 (2013).
55. Katz, M. J. *et al.* A facile synthesis of UiO-66, UiO-67 and their derivatives. *Chem. Commun.* **49,** 9449–9451 (2013).
56. Valenzano, L. *et al.* Disclosing the Complex Structure of UiO-66 Metal Organic Framework: A Synergic Combination of Experiment and Theory. *Chem. Mater.* **23,** 1700–1718 (2011).
57. Chui, S. S.-Y., Lo, S. M.-F., Charmant, J. P. H., Orpen, A. G. & Williams, I. D. A Chemically Functionalizable Nanoporous Material [Cu3(TMA)2(H2O)3]n. *Science* **283,** 1148–1150 (1999).
58. P. P. Ewald. *Fifty Years of X-Ray Diffraction*. (International Union of Crystallography, 1962). at <http://iucr.org>
59. H. S. Lipson. William Lawrence Bragg. *Acta Crystallogr. Sect. A* 1890–1971
60. Report of the Executive Committee for 1991. *Acta Crystallogr. Sect. A*
61. *International Tables for Crystallography: Space-group symmetry*. **A,** (International Union of Crystallography, 2006).
62. Reyleigh, L. The explanation of certain acoustical phenomena. *Nature* **18,** 319–321 (1878).
63. Thibault, P. & Elser, V. X-Ray Diffraction Microscopy. *Annu. Rev. Condens. Matter Phys.* **1,** 237–255 (2010).
64. Bragg, W. L. The diffraction of short electromagnetic wave by a crystal. *Proc. Camb. Philos. Soc.* (1914).
65. Pecharsky, V. K. & Zavalij, P. Y. *Fundamentals of powder diffraction and structural characterization of materials*. (2005).
66. Authier, A. *The Reciprocal Lattice*. (International Union of Crystallography, 1981).
67. Authier, A. *Dynamical Theory of X-ray Diffraction*. (Oxford University Press, 2004).
68. Guinier, A. *X-ray Diffraction in Crystals, Imperfect Crystals, and Amorphous Bodies*. (Courier Dover Publications, 1994).
69. Hammond, C. *The Basics of Crystallography and Diffraction*. (Oxford University Press, 2009).
70. Zou, X., Hovmöller, S. & Oleynikov, P. *Electron Crystallography: Electron Microscopy and Electron Diffraction*. (Oxford University Press, 2011).
71. Cooper, E. R. *et al.* Ionic liquids and eutectic mixtures as solvent and template in synthesis of zeolite analogues. *Nature* **430,** 1012–1016 (2004).

72. Su, J. *et al.* Structure analysis of zeolites by rotation electron diffraction (RED). *Microporous Mesoporous Mater.* **189,** 115–125 (2014).
73. Stokkebro Schmøkel, M. *et al.* Pushing X-ray Electron Densities to the Limit: Thermoelectric CoSb3. *Angew. Chem. Int. Ed.* **52,** 1503–1506 (2013).
74. Liu, L., Li, M., Gao, W., Åkermark, B. & Sun, J. Structure determination of [3Fe2S] complex with complicated pseudo-merohedric twinning. *Z. Für Krist. Cryst. Mater.* **227,** 221–226 (2012).
75. Sheldrick, G. M. A short history of SHELX. *Acta Crystallogr. A* **64,** 112–122 (2007).
76. David, W. I. F. *Structure Determination from Powder Diffraction Data*. (Oxford University Press, 2002).
77. Gilmore, C. J., Shankland, K. & Bricogne, G. Applications of the Maximum Entropy Method to Powder Diffraction and Electron Crystallography. *Proc. Math. Phys. Sci.* **442,** 97–111 (1993).
78. Černý, R. & Favre-Nicolin, V. Direct space methods of structure determination from powder diffraction: principles, guidelines and perspectives. *Z. Für Krist.* **222,** 105–113 (2007).
79. Oszlányi, G. & Sütő, A. *Ab initio* structure solution by charge flipping. *Acta Crystallogr. A* **60,** 134–141 (2004).
80. Wu, J. S., Spence, J. C. H., O'Keeffe, M. & Groy, T. L. Application of a modified Oszlányi and Sütő *ab initio* charge-flipping algorithm to experimental data. *Acta Crystallogr. A* **60,** 326–330 (2004).
81. Wu, J., Leinenweber, K., Spence, J. C. H. & O'Keeffe, M. Ab initio phasing of X-ray powder diffraction patterns by charge flipping. *Nat. Mater.* **5,** 647–652 (2006).
82. Baerlocher, C., McCusker, L. B. & Palatinus, L. Charge flipping combined with histogram matching to solve complex crystal structures from powder diffraction data. *Z. Für Krist.* **222,** 47–53 (2007).
83. Kolb, U., Gorelik, T., Kübel, C., Otten, M. T. & Hubert, D. Towards automated diffraction tomography: Part I—Data acquisition. *Ultramicroscopy* **107,** 507–513 (2007).
84. Zhang, D., Oleynikov, P., Hovmoller, S. & Zou, X. Collecting 3D electron diffraction data by the rotation method. *Z. Krist.* **225,** 94–102 (2010).
85. Martínez-Franco, R. *et al.* Synthesis of an extra-large molecular sieve using proton sponges as organic structure-directing agents. *Proc. Natl. Acad. Sci.* **110,** 3749–3754 (2013).

86. Guo, P. *et al.* Ab initio Structure Determination of Interlayer Expanded Zeolites by Single Crystal Rotation Electron Diffraction. *Dalton Trans.* doi:DOI:10.1039/C4DT00458B
87. Zhang, Y.-B. *et al.* Single-Crystal Structure of a Covalent Organic Framework. *J. Am. Chem. Soc.* **135,** 16336–16339 (2013).
88. Han, Y. *et al.* A tri-continuous mesoporous material with a silica pore wall following a hexagonal minimal surface. *Nat. Chem.* **1,** 123–127 (2009).
89. Sun, J. *et al.* Structure determination of the zeolite IM-5 using electron crystallography. *Z. Für Krist. Int. J. Struct. Phys. Chem. Asp. Cryst. Mater.* **225,** 77–85 (2010).
90. Gramm, F. *et al.* Complex zeolite structure solved by combining powder diffraction and electron microscopy. *Nature* **444,** 79–81 (2006).
91. Bonneau, C. *et al.* Open-Framework Germanate Built from the Hexagonal Packing of Rigid Cylinders. *Inorg. Chem.* **48,** 9962–9964 (2009).

8 Appendix

Table 8.1 Seven crystal systems and the corresponding symmetry requirement and unit cell restrictions.

Crystal system	required symmetry	unit cell restriction	Bravais lattice
Triclinic	none	$\alpha, \beta, \gamma \neq 90^o$ [1]	Triclinic
Monoclinic	a 2-fold rotation axes or mirror plane along one direction	$\alpha, \gamma \neq 90^o; \beta = 90^o$	Primitive Monoclinic C-centred Monoclinic
Orthorhombic	three 2-fold rotation axis or mirror planes along three direction	$\alpha, \beta, \gamma = 90^o$	Primitive Orthorhombic C-centred Orthorhombic I-centred Orthorhombic F-centred Orthorhombic
Tetragonal	a 4-fold rotation axes along one direction	$a = b \neq c;$ $\alpha, \beta, \gamma = 90^o$	Primitive Tetragonal I-centred Tetragonal
Trigonal	a 3-fold rotation axes along one direction	$a = b \neq c;$ $\beta = 120^o; \alpha, \gamma = 90^o$ [2]	Rhombodedral
Hexagonal	a 6-fold rotation axes along one direction	$a = b \neq c;$ $\beta = 120^o; \alpha, \gamma = 90^o$	Hexagonal
Cubic	three 4-fold rotation axes along one direction	$a = b = c;$ $\alpha, \beta, \gamma = 90^o$	Primitive Cubic I-centred Cubic F-centred Cubic

1. *The Symbol ≠means "doesn't have to be";*
2. *When the trigonal structure is R-centered, there are the other setting of trigonal unit cell: a=b=c;α=β=γ≠90o.*